The Contribution of Glacial Isostatic Adjustment to Past and Contemporary Relative Sea-Level Rise along the Atlantic Coast of Europe

by

Geoffrey Alan Chapman

A thesis submitted in partial fulfillment of the requirements
for the
Master's degree in Earth Sciences

Department of Earth and Environmental Sciences
University of Ottawa
Ottawa, Ontario, Canada

Supervised by:

Prof. Glenn A. Milne, *University of Ottawa, Ontario, Canada*

Abstract

Contemporary and future relative sea-level (RSL) rise that can be attributed to anthropogenic climate change sees significant spatial variability as a result of the processes that underlie it. Some of the processes that contribute to RSL rise unrelated to anthropogenic climate change can and have had significant contributions. In this work, we examined the contributions of one of these processes, glacial isostatic adjustment (GIA), in the coastal regions of Atlantic Europe. These regions have seen significant RSL rise associated with a collapsing peripheral bulge throughout the Holocene and are expected to see more throughout the Anthropocene. Using the recently published paleo sea level database (García-Artola et al., 2018) which follows the HOLSEA RSL data assessment and reporting protocol (Khan et al., 2019) we determined optimal Earth model parameters for much of Atlantic Europe. These optimal parameters fit the data well and largely agree with values determined for previous works on peripheral bulges along the coasts of North America. We further used these results to perform a rudimentary sea-level budget analysis at 10 tide gauge stations, yielding results with high uncertainties and significant discrepancies between observed and projected rates of RSL change for half (5) of the tide gauge stations. Our results lead to the conclusion that GIA remains an important factor when predicting present and future RSL change.

Table of Contents

List of Figures

List of Tables

List of Abbreviations

ANU	Australian National University (global ice history model, from)
ASL	Absolute Sea Level
EM	Earth Model
FIS	Fennoscandian Ice Sheet & a set of regional ice history models
GHG	GreenHouse Gas
GIA	Glacial Isostatic Adjustment
GMSL	Global Mean Sea Level
GPS	Global Positioning System
HOLSEA	HOLocene relative SEA level (initiative)
ICE-6G	ICE-6G(C) (global ice history model)
LGM	Last Glacial Maximum
LMV	Lower Mantle Viscosity
LT	Lithospheric Thickness
ML	Marine Limiting
NGL	Nevada Geodetic Laboratory
PSMSL	Permanent Service for Mean Sea Level
RRSL	Rate of RSL
RSL	Relative Sea Level
SLIP	Sea Level Index Point
TL	Terrestrial Limiting
UMV	Upper Mantle Viscosity
VLM	Vertical Land Motion

Preface

Some portions of calculations were run by colleagues from within *Glenn A. Milne*'s working group at the *University of Ottawa*, namely *Parviz Ajourlou* who performed the best linear unbiased estimation (BLUE) in Section 2.3.2.2, *Soran Parang* who provided nominal Bayesian projections for optimal Earth parameter sets, *Ryan Love* who provided a cleaner .xy file when the original version created proved inadequate, and *Glenn A. Milne* who provided the GRD files corresponding to optimal Earth model parameters as well as extensive feedback on and suggestions on drafts. *Lev Tarasov* supplied regional ice models relevant to our study region for use in modelling GIA. *Glenn A. Milne, Parviz Ajourlou, Soran Parang,* and *Lev Tarasov* have contributed meaningfully to the second chapter of this work and will be credited as such should it be submitted to a scientific journal for publishing.

The results presented in this work were generated using programs written in Fortran, Python, and Unix shell-scripts. Fortran and Unix scripts were compiled using SSH Secure Shell for Windows, while Python scripts were compiled using JetBrains' PyCharm Community Edition 2020.3.3. The figures found in this work were composed using Generic Mapping Tool (GMT v4.5.15; Wessel and Smith, 1991) and the aforementioned PyCharm with modifications made using Windows' Paint 3D.

Acknowledgements

I would like to thank my supervisor, Glenn Milne, for his role in seeing this work to completion. Your expertise and guidance have proved invaluable, and you have remained a patient and quite approachable supervisor throughout this entire labour.

I would also like to thank members of my working group, for sharing codes, data, and expertise in one form or another. In particular I would like to thank Soran Parang for his occasional refresher in Python for scientific use and his help with nominal Bayesian statistics computations, Parviz Ajourlou for some statistical analysis beyond my wheelhouse, and Ryan Love for the use of some of his code.

Gratitude must also be extended to my father, Kevin Chapman, for supporting me in many ways over these long pandemic years.

Chapter 1: Introduction

1.1 Motivation

The 20th century has seen global mean sea level (GMSL) rise faster than in any century of the last 3000 years (Fox-Kemper et al., 2021). This roughly 3000 year long period of relative sea level (RSL) quiescence proved to be a window of opportunity for humanity to increasingly settle in coastal areas to take advantage of access to the oceans – advantages such as resources, amenities, transit, and flat topography seen in geographic locations such as alluvial plains and deltas – particularly with regards to industrialisation and globalisation of trade. However, much of this is threatened by ongoing anthropogenic climate change with settlements and entire sectors of local and global economies coming under threat (IPCC 2023: Summary for Policy Makers). Coastal wetlands for instance, which often protect inhabited areas, have seen global losses of up to 70 % since the beginning of the 20th century (Davidson, 2014).

Having consistently seen population growth over time (roughly 40 % of the world's population lives in areas considered coastal), coastal areas are expected to see additional growth into the future. European coastal populations were estimated at 308 million in 2020 and projected to reach 311 million by 2035 (Maul & Duedall, 2019). Meanwhile, expected annual damages from flooding in Europe are expected to rise from 1.25 billion in 2018 to 93-961 billion by the end of the century (Vousdoukas et al., 2018).

Given this threat to coastal populations and infrastructure, creating accurate predictions of sea-level rise is an important scientific endeavour. This issue is made more complex as changes in sea level vary considerably from changes to GMSL (see Figure 1.1). While determining GMSL is complicated because of the need to sum changes in ocean density due to salinity and temperature changes, and changes in ocean mass from inputs and outputs of water (Fox-Kemper et al., 2021), RSL is more complicated. Rates of RSL change can be affected by changes in gravity (and rotation of the Earth), in ocean and atmospheric circulation, local ground motion effects (fluid extraction, tectonism, compaction, etc.), and solid Earth processes (Stammer et al., 2013). These solid Earth processes are of particular interest to this work with glacial isostatic adjustment – the response of the solid Earth, the gravitational field, and the oceans to changes in size and location of ice sheets (Whitehouse, 2018) – being an important contributor to sea-level change in regions previously covered by and those peripheral to said regions (Harvey et al.,

2021; Love et al., 2016). In this thesis, we focus on the contribution of GIA to sea-level change along the Atlantic coast of Europe, which has seen significantly less examination of the effects of GIA compared to North America.

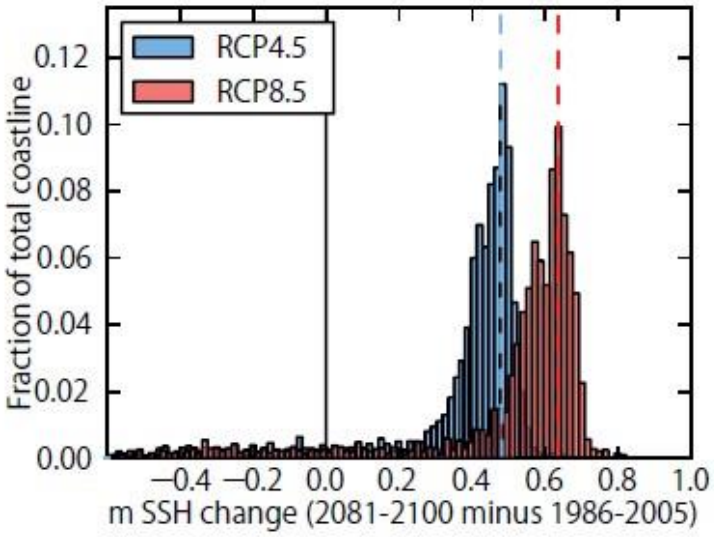

Figure 1.1. Histograms of the deviation of the ensemble mean RSL change along all coastlines between 1986-2005 and 2081-2100 from the global mean value. Shown are Representative Concentration Pathway (RCP) 4.5 (blue) and 8.5 (pink), see the International Panel on Climate Change's Assessment Report 5 for details (modified from Church et al., 2013).

1.2 Defining and Observing Sea-Level Change

As with many other concepts ranging from the taxonomical or philosophical to the physical, "sea level" seems intuitive at first blush but proves to be more complex upon closer examination. RSL can be fairly easily defined as the distance between the sea surface and the ocean floor beneath it with the latter as our reference surface (see Figure 1.2). Both of these distances, the distance of the ocean floor and the sea surface to the centre of the Earth, can change, e.g. with tectonic movement or local subsidence for the former, and climatic factors for the latter (Sections 1.3, 1.4). Absolute sea level (ASL) (Figure 1.2) is sea-surface height measured relative to the reference ellipsoid of the Earth. The reference ellipsoid is a mathematically defined surface that most closely approximates the geoid. The geoid is a theoretical surface that approximates where the mean sea surface (ignoring tides, etc.) would be under the influence of the Earth's gravitational and centripetal forces (Milne, 2014).

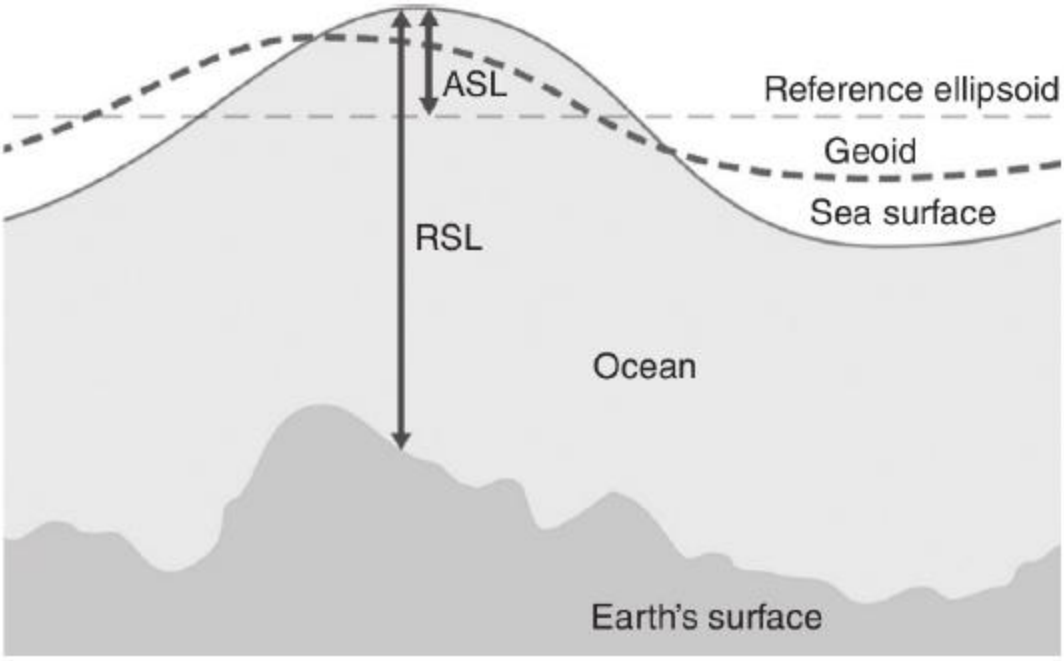

Figure 1.2. Relative sea level (RSL) defined as the height between the sea surface and the Earth's surface (the sea floor). The geoid is an equipotential surface of the Earth's gravity field approximating the mean position of the ocean surface over a multi-decadal time period. The reference ellipsoid is the mathematical surface that best fits this surface. Absolute sea level (ASL) or geocentric sea level is the height of the sea surface relative to this reference ellipsoid. (Milne, 2014).

Various methods for measuring contemporary sea level have been used throughout human history, with tide gauge data (which records and averages the height of the water column at specific locations over specific time intervals, ideally anchored in bedrock to reduce signal noise) being the primary source since ~1880 (e.g., Holgate et al., 2013). Tide gauges provide measurement of RSL. The age of satellite altimetry (1993-present) has since begun, allowing for accurate measurements of sea-level change across the globe. This method provides measurements of absolute sea level.

ASL measurements are useful for assessing changes to sea level associated with climate change (often GMSL), but is overshadowed in terms of utility by RSL measurements when determining present and future effects of sea-level change as RSL includes vertical land motion which makes it a more complete measure of sea-level change. The movement of the Earth's crust can and does have significant effects on coastal communities, for instance subsidence can threaten said

communities with rising sea levels when the sea surface relative to the reference ellipsoid is not significantly changing (Milne, 2014).

1.2.1 Reconstructing Past Relative Sea Level

As with determining where relative sea level is in the present or will be in the future, there are complications when determining where it was in the past. The paleorecord needs to be reconstructed using sea level index points (SLIPs) and/or limiting data, which are, respectively, estimates of the height of RSL in space and time, and estimates of positions that constrain RSL above or below their height in space and time (Figure 1.3). This allows us to create sea-level curves, see Section 1.5. These RSL heights in time and space are effected by a degree of uncertainty on both the height and time axes based on their marker type, methods of dating, etc., which will be touched on in this section.

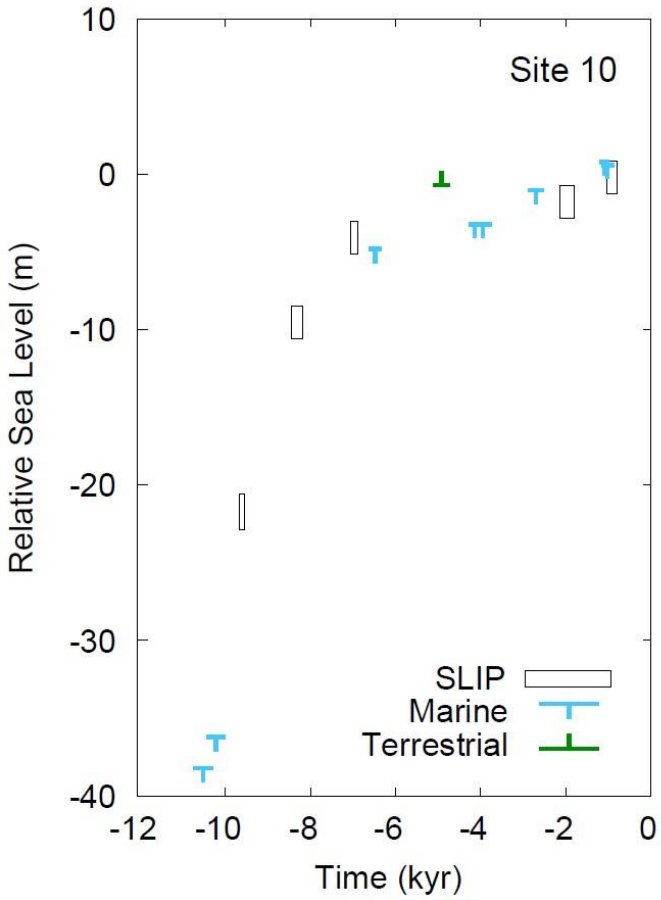

Figure 1.3. Example of paleo RSL data types (see key) used in this study.

A sea level index point can be defined using surviving indicators of ancient RSL such as in situ sediments, fossil organisms, or features (morphological/archeological) that were controlled by paleo sea level. In brief, they are indicators that, based on contemporary conditions, indicate where sea level was in the past such as tidal pools, lagoonal deposits, coastal karst basins, lagoonal corals, etc. (Shennan, 2015; Harvey, 2015).

Whereas SLIPs provide relatively precise height constraints on past RSL (sea level must pass through the defined height range within the time period they encompass), limiting data constrain sea level precisely in only one vertical direction. For instance, many plant macrofossils are from plants that could not exist in salt-water conditions and thus indicate sea level was below that datum, while deep-sea corals or other sub-marine indicators constrain sea level to above their depth while they were living.

RSL measurements come with varying degrees of uncertainty, which is introduced in many ways. For example, during field sampling such as when coring (inherent margin of uncertainty in measuring instruments, uncertainty from unideal measuring conditions, operator error, etc.), due to imprecision inherent in an indicator based on its type (tidal fluctuations have a vertical range, as do high vs low stand salt marshes, etc.), or processes that affect position in time and space between the time of deposition and burial but pre-recording of the measurement such as bioturbation of sediment layers (Woodroffe et al., 2015).

Radiocarbon dating using the radioactive C^{14} isotope is capable of dating organic material such as shells and surviving plant matter including pollen up to roughly 60,000 years into the past. However, dates calculated using this method need to recalibrated due to local variations in carbon isotope concentrations, such effects as the marine reservoir effect, and fractionation of heavier isotopes (e.g. by heterotrophs through predation of foraminifera, diatoms, etc.). As C^{14} decays into C^{13}, carbon dating must be adjusted based on ratios of C^{13}/C^{12} in the sample being dated, based on expected values as these vary depending on what source acts as input into the system from which the sample is collected. C^{13}/C^{12} ratios are calculated using Equation 1, where $\delta^{13}C$ values are measured in ‰, C^{13}/C^{12} of the sample is the ratio of isotopes for the sample being analysed while C^{13}/C^{12} standard is the ratio for natural inorganic carbon.

$$\delta^{13}C = \frac{{}^{13}C/{}^{12}C_{sample} - {}^{13}C/{}^{12}C_{standard}}{{}^{13}C/{}^{12}C_{standard}} \times 1{,}000 \qquad \text{(Eqn. 1)}$$

The ocean is generally expected to have $\delta^{13}C$ values approaching 0‰, while terrestrial plant matter is expected to have values closer to -27‰ (as were used as the defaults in García-Artola, et al., 2018). Differences in the ratio of C^{13}/C^{12} for meteoric or ocean water when compared to plant matter are so different due to plants fractionating out C^{13} slightly during photosynthesis (Ruddiman, 2014).

1.3 Processes Affecting Sea-Level Change

The Earth's climate, and thus sea level, fluctuates on a wide range of timescales (e.g., Ruddiman, 2014). For example, over 10s-100s kyr, orbital changes are important (Milanković, 1941); on longer timescales, plate tectonic and mantle dynamic effects (Yokoyama and Purcell, 2021) become more important. These fluctuations affect sea level in multiple ways. As an example, climatic changes directly impacting how much water is sequestered in ice sheets (more on the effects of ice-loading later in this section and in Section 1.4), delayed dynamic effects such as land motion caused by different loading of the Earth's crust (ocean and ice loading, etc.), and various other geophysical processes. The Earth's climate has warmed over the last 10,000 years and more (largely under the effects of orbital mechanics), previously reaching a multi-century peak sometime during the current interglacial period, around 6,500 years ago (IPCC, 2023: Synthesis Report). This change is caused by slow, orbital changes rather than the more recent warming attributed to anthropogenic climate change (IPCC 2023: Summary for Policy Makers). Sea level had risen and roughly stabilised at present-day levels around 6,500 years before present. The rate of GMSL rise has risen dramatically since the Industrial Revolution, with the average annual rate between 1901 and 1971 being ~1.3 mm/yr, increasing to a rate of 1.9 mm/yr between 1971 and 2006, and 3.7 mm/yr between 2006 and 2018 (IPCC 2023: Summary for Policy Makers).

GMSL and RSL are both affected by density changes. These changes comprise the steric component of sea-level change, affecting the height of the water column. This component can be broken into the thermosteric and halosteric changes in ocean water. The thermosteric component affects ocean volume as warmer water is less dense and occupies a greater volume. Colder water is generally denser, but due to quirks associated with the chemistry of pure water, minimum density occurs at 4 ºC, with water ice being less dense than liquid water. It is also worth remarking that the abundance of water on the Earth has led to ~91 % of the climate system's

total warming due to anthropogenic climate change being to the surface layers of the ocean (0-700 m). The remainder of this heat being stored in the atmosphere, cryosphere, and land (IPCC 2023: Summary for Policy Makers). The halosteric component refers to the density effects resulting from changes in water salinity. Such effects as the influx of freshwater (glacial, riverine, etc.) reduce salinity. The solubility of salts does not increase significantly with ocean warming, particularly not compared with other compounds. Figure 1.4 depicts the variation between the geoid and the time-averaged ocean surface, with a clear contribution from thermosteric and halosteric effects (e.g., lower in the Southern Ocean, a higher sea surface at lower latitudes, etc.).

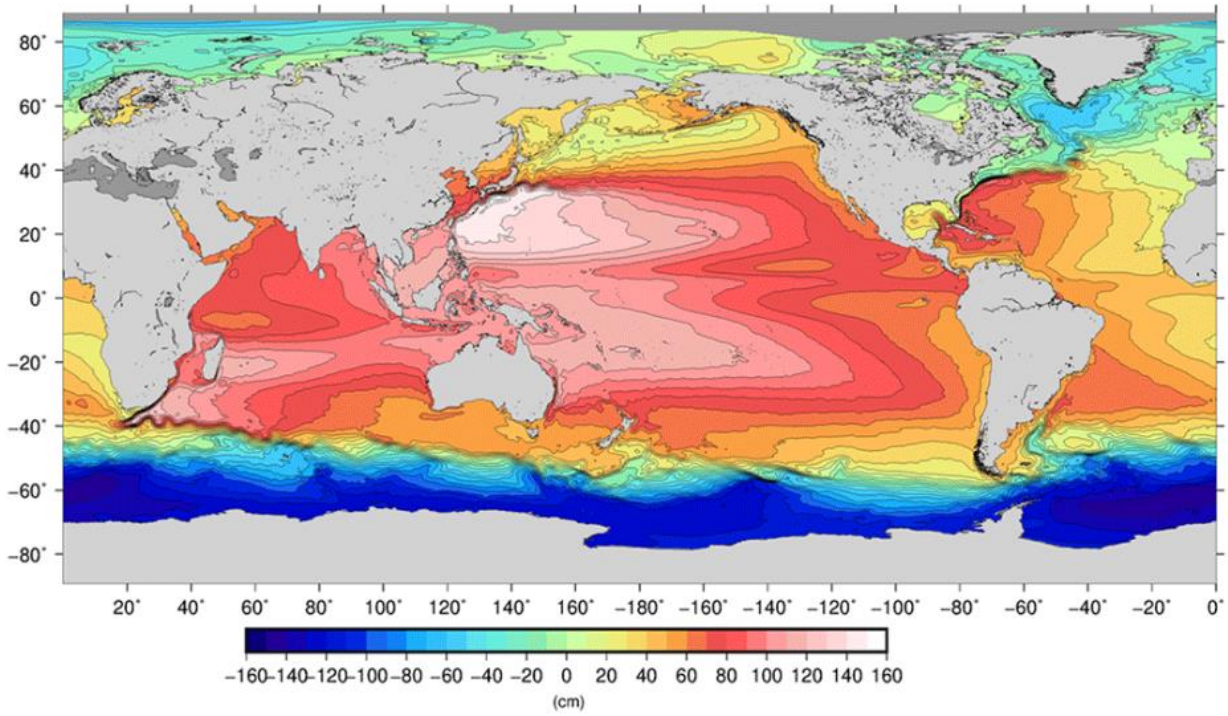

Figure 1.4. Mean Dynamic Ocean Topography (difference between time-averaged ocean surface and geoid) for CNES-CLS18. (Mulet, S., et al., 2021).

Hydrological factors such as storage (impoundment) and extraction from aquifers (groundwater mining) can affect sea level to an extent by affecting flow into basins through many processes. Anthropological examples include the mixed effects of urbanization (greater run-off, decreases in infiltration leading to greater flow to basins), aquifer compaction (reduction in storage space once groundwater is extracted leading to subsidence), reduced riverine inputs for agricultural

purposes (irrigation reducing inputs), increased inputs due to deforestation, etc. (Gornitz, 2001, Douglas, 2001). These signals have varying levels of importance depending on location, but on a global scale are a relatively small factor (~0.9 ± 0.5 mm/yr in 2001 per Douglas, 2001).

Finally, of the important and relevant factors affecting sea-level change, ice (glaciers, etc.) affects sea level in many ways (covered in greater detail in Section 1.4). Contributions include directly through melting or sequestration as previously mentioned, but also includes processes that affect the shape of the geoid (and thus the distribution of ocean water), the Earth's rotation, and the shape of the solid Earth.

1.4 Glacial Isostatic Adjustment & Related Processes

As previously mentioned, the Earth undergoes quasi-periodic changes in climate due to multi-millennial orbital forcings. At a minimum, there have been some five major ice ages in the Earth's past that have been identified in paleo records and denoted by permanent terrestrial ice sheets. Each ice age is marked by glacial and interglacial periods. Glacial periods denoted by periods of cooler global temperatures and advancing ice sheets, while interglacial periods are marked by warmer periods in which ice sheets retreat or disappear completely. The most recent of these glacial periods peaked around 21,000 years ago at the last glacial maximum and terminated around 11,700 years ago. During this time, massive ice sheets grew to cover much of North America and Eurasia, with the last glacial maximum marking the furthest extent (Ruddiman, 2014).

Glacio-isostasy

The massive ice sheets in place during the last glacial period naturally exerted a stress on the surface of the Earth. Such "ice loading" causes the Earth to deform viscoelastically. That is to say, when experiencing crustal loading, the Earth experiences an immediate elastic response followed by a larger, slower and sustained, viscous response as the mantle is forced into a new equilibrium due to the overlying weight. The last glacial maximum marked the greatest extent, prior to the present, for these ice sheets and their greatest thickness and thus marking a similarly large downward deflection of the lithosphere under the weight of the overlying ice. For such a glacial event as the last glacial period, recovery to the new equilibrium point post deglaciation can be expected to be measured in the tens of thousands of years. In addition to a downward

deflection of the Earth's surface directly beneath them, ice sheets create a much smaller upward deflection along their margins termed a "peripheral bulge" (see Figure 1.5). Although the long-term GIA signal is significantly smaller than the barystatic signal associated with the initial melting event (as a global average), the smaller long-term effect of GIA makes past glacial loading events relevant to understand observations of RSL change and vertical land motion (Conrad, 2013, Love et al., 2016; Yousefi et al., 2018). An area on a subsiding peripheral bulge will see an increased RSL rise rate. The GIA component of RSL change has dominated during the past ~20 kyr and it and continues to be an important contributor in regions once covered or adjacent to ancient ice sheets (Milne et al., 2005; Love et al., 2016).

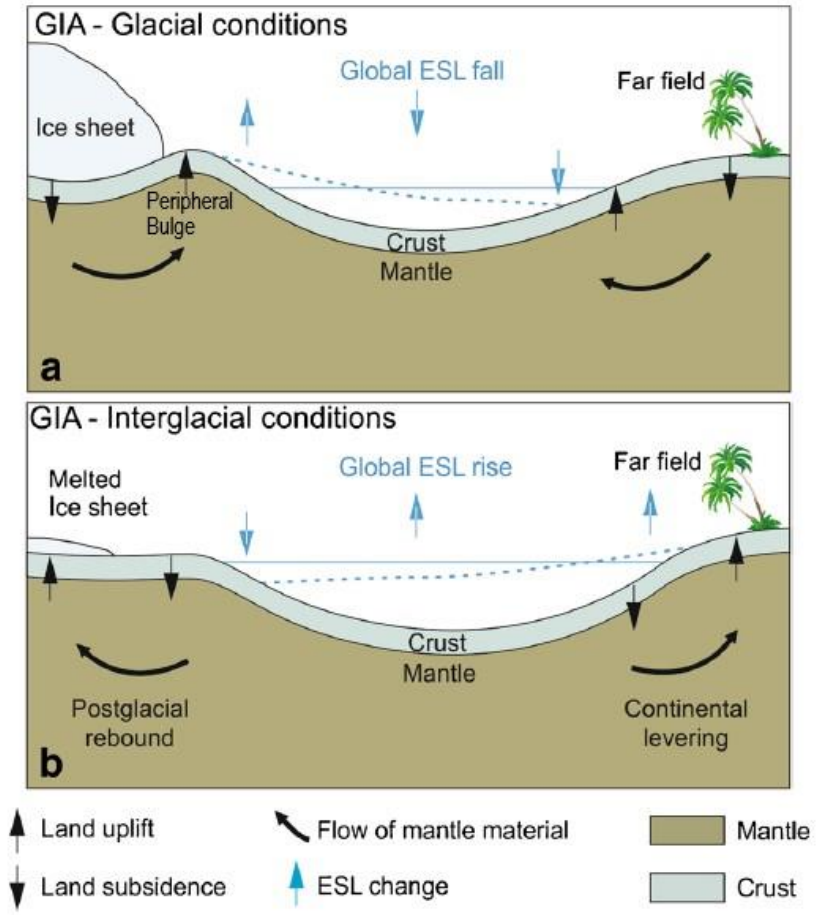

Figure 1.5. Schematic of isostatic responses of the Earth's mantle and crust to present and past masses. a) shows near-field effects (left) of a present glacial mass, and how the Earth deforms under the weight, and far-field effects (right) resulting from gravitational changes are shown. b) shows the gradual relaxing of deformation as the system shifts further towards isostatic equilibrium (in this case, significant reduction of glacial mass). Continental levering is depicted (right) due to hydro-isostatic loading. Not depicted, a fully relaxed state. "ESL change" refers to Eustatic Sea-Level change, i.e. change driven by changes in mass or volume of water (adapted from Rovere et al., 2016).

Hydro-isostasy and rotational effects

The ocean surface approximates the geoid on long time scales (10s-100s of years), which results in more water being drawn towards areas with large ice sheets (e.g. during glacial periods) and away from areas further away from ice sheets, which contributes to ocean loading (the larger signal being the barystatic contribution or eustatic sea level). As with ice loading, ocean loading causes a deformation of the underlying viscoelastic Earth. When ice sheets retreat, the ocean surface is quick to respond with water proximal to former ice sheets flowing to areas distant from them. This results in immediate RSL fall proximal to where ice sheets were, and some RSL rise in the far-field. The slight uplift on the margins of Africa and Australia in Fig. 1.6 is caused by the ocean-loading post deglaciation levering up continental mass (this is termed "continental levering" in works such as Clark et al., 1978, see Fig. 1.5). This has a more obvious far-field effect, in large part because as a near-field effect hydro-isostasy is overshadowed by glacio-isostasy. The effects of hydro-isostasy are significantly smaller than the effects of ice loading, roughly an order of magnitude lower (Milne & Shennan, 2013). As mentioned however, the response of oceans to changes in mass and topography are rapid and cannot be dismissed when attempting to model how the Earth responds.

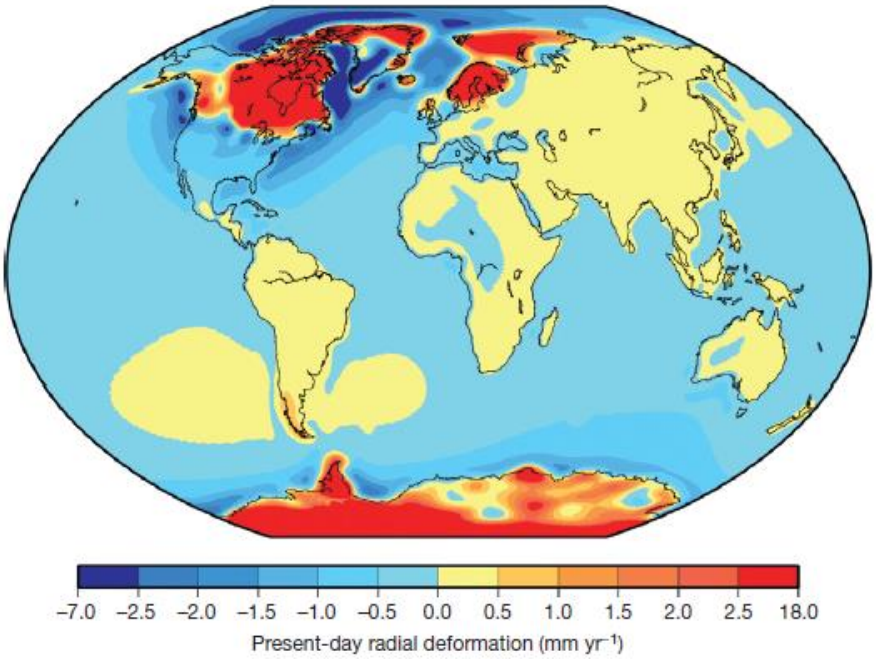

Figure 1.6. Present-day vertical land motion based solely on GIA influence in 2004 as predicted using deglaciation history ICE-5G (Peltier, 2004) from Milne & Shennan (2013).

The massive amount of water that was contained within terrestrial ice sheets as previously described amounted to ice sheets that were kilometers thick in some places. These ice sheets were large enough to significantly impact the shape of the geoid and alter the rotational axis of the Earth (tilt and spin rate). These effects can also affect rates of RSL change and thus are included in sea-level models (Milne & Mitrovica, 1998). Figure 1.6 depicts the modeled combined effects of GIA (glacio- and hydro-isostasy, and rotational effects) to the Earth based on the ice-loading history ICE-5G (more on ice-loading histories in Section 1.5).

1.5 Modeling GIA

In order to constrain the GIA signal to accurately predict future change, one must have an Earth model that predicts responses to loading and unloading of the Earth's surface. One such model commonly used in GIA modelling is a spherically symmetric, Maxwell rheology Earth model as presented in Peltier (1974). Another required model component is a space-time history of the global ice sheets (some details of which are reconstructed from observations of past ice sheet extents, etc.).

When modelling GIA, not only must the ice history be included as an input and the rheology of the solid Earth, but also changes to the shape and distribution of the ocean basins that occur as ice sheets change in size and deform the solid Earth and perturb the geopotential. The resulting sea-level changes are computed by solving the sea-level equation as originally presented in Farrell and Clark (1976). A generalized version of the sea-level equation can be found in Mitrovica and Milne (2003). Figure 1.7 presents how GIA models must consider the behaviour of the solid Earth, the oceans, and the ice sheets upon the Earth. The Earth's rheology as well as the aforementioned space-time history of ice sheets are informed by real-world observations while changes to the shape of the ocean and the solid Earth being solved by the aforementioned sea-level equation (Whitehouse, 2018). When computed by the GIA model, outputs include sea-level change and solid Earth deformation and other aspects of the Earth system (see Figure 1.7 "Outputs"). Changes in sea level, the geoid, rotational effects, the shape of the Earth etc. all impact loading, i.e. the inputs, creating an iterative process in which outputs are compared to real-world observations, and adjustments to ice and Earth models are adjusted as needed.

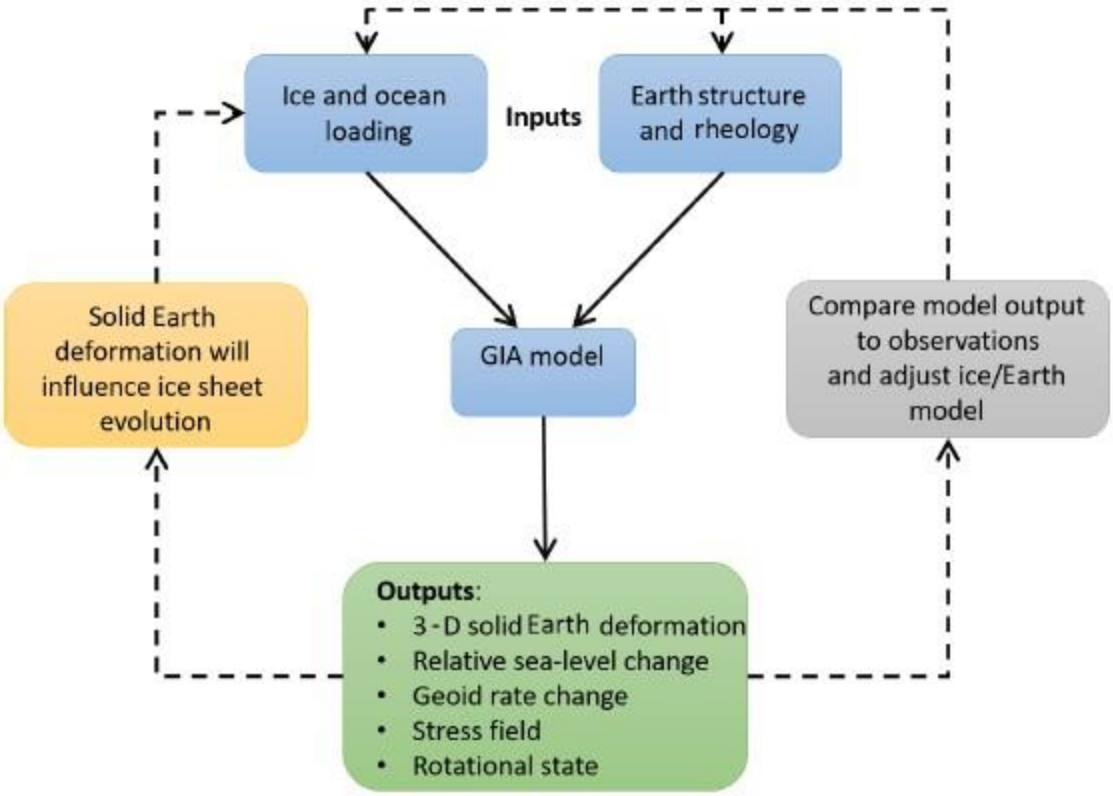

Figure 1.7. The components of a GIA model (modified from Whitehouse, 2018). Major inputs are surface loading by ice sheets (based on ice history model) and the ocean, and Earth properties. These impact how the solid Earth deforms, and provides the outputs listed. Solving the sea-level equation provides changes to the gravity field of the Earth (and thus the geoid) which in turn dictates how meltwater is redistributed in the oceans, altering ocean loading. The changes in loading and deformation feed back into inputs. The results are compared to real-world observations and adjustments are made as necessary to improve results.

1.6 Thesis Aims

It is important to better constrain the contributions of GIA to present and future RSL change particularly in regions experiencing GIA-related subsidence (e.g. those regions located on a peripheral bulge) as this subsidence contributes to sea-level rise. The contribution of GIA to sea-level rise in North America has been relatively well constrained (e.g. Roy and Peltier, 2015; Love et al., 2016; Yousefi et al., 2018; Harvey et al. 2021), but there is a lack of similar studies for the Atlantic Coast of Europe, despite the knowledge that it is also a region experiencing subsidence (Leorri et al., 2012; Goslin et al., 2015; García-Artola et al., 2018). The focus of this work, therefore, is to make use of more complete RSL (García-Artola et al., 2018) and vertical land motion (Schumacher et al., 2018) datasets that have been recently published to constrain a

large Earth and ice model parameter set and thus better quantify the contribution of GIA to RSL and land motion along this highly populated coastline.

Chapter 2: Modelling GIA and its Effects on Past, Present, and Future RSL Change

2.1 Introduction

Anthropogenic climate change continues to produce sea-level rise through global climate warming at an accelerating rate (Fox-Kemper et al., 2021). It is thus important to better understand and quantify contributions to contemporary and future sea-level change. One route to this goal involves considering records of ice-sheet and sea-level changes since the Last Glacial Maximum (LGM) with an aim to better understand the deglaciation process and its effects on sea level. Not only does this route provide a better understanding of the most recent deglaciation event and the underlying processes, this major climate transition continues to impact changes in sea level both globally and locally through the process of glacial isostatic adjustment (GIA). Sea-level change is a composite signal, with components such as thermosteric and halosteric changes, water fluxes, and land motion (Slangen et al., 2012). These processes occur on a variety of spatial and temporal scales, and GIA is an important contributor to secular changes in the land motion component.

GIA is the response of the solid Earth to past surface loading associated with ice-ocean mass transfer (for example, Peltier, 1999) and is known to be more significant in regions proximal to the late Quaternary ice sheets, such as in North America, Northern Europe, and Fennoscandia (Hammond et al., 2021). In most regions once covered by past ice sheets, GIA results in contemporary upward vertical land motion (VLM), while in areas near or beyond the LGM ice margins, GIA results in downward VLM (e.g., Peltier, 1996; Peltier, 2004). This latter area is referred to as the peripheral bulge, where subsidence is observed during most of the deglaciation and in contemporary times (Muhs et al., 2012; Goslin et al., 2015). Local rates of contemporary sea-level change can vary wildly from the global average – ~20 % from median projected global mean sea level (GMSL) rise (Fox-Kemper et al., 2021) – due to various factors including the GIA signal, which is contributing to contemporary sea level by increasing or decreasing rate of fall or rise (Love et al. 2016; Karegar et al., 2016). Quantifying the GIA contribution to current and future sea-level change is important, particularly in peripheral bulge regions where it generally enhances the other component signals.

It is important to have robust paleo sea-level data against which GIA models can be validated (Gehrels et al., 2011). These models use information on the regional and global ice history, and Earth rheology to calculate the GIA-related sea-level changes (Farrell and Clark, 1976, Whitehouse, 2018). The modelled changes are then compared to observations to determine a parameter set that minimises the data-model misfit (e.g., Peltier and Andrews, 1976; Lambeck et al., 1998; Simpson et al., 2009; Tarasov et al., 2012; Roy and Peltier, 2015). In the past decade there has been a focused community effort to produce regional relative sea level (RSL) databases in a standardised format (Khan et al., 2019) which has led to a growing number of high-quality databases being made available to constrain GIA models (e.g., Love et al., 2016; Yousefi et al., 2018; Li et al., 2020). A recently published dataset for the Atlantic coast of Europe (García-Artola et al., 2018), which is part of this community effort (known as the HOLocene relative SEA level (HOLSEA) initiative), motivated and enabled the GIA modelling study presented in this paper.

Previous works have explored the effects of GIA on sea-level change in North America on both eastern (Davis and Mitrovica, 1996; Wake et al., 2006; Engelhart et al., 2009; Roy and Peltier, 2015; Love et al., 2016) and western coasts (James et al., 2009; Yousefi et al., 2018). Love et al. (2016) estimate a rise of 3-18 cm between 2000 and 2100 CE across the region which covers the eastern and Gulf coasts of North America from St John's, Newfoundland, Canada, to Galveston, Texas, USA with the higher contributions to RSL rise generally being found in the more northerly parts of this coastline. In the western parts of North America, Yousefi et al. (2018) found contributions from GIA to RSL between 2010 CE and 2100 CE ranging from a drop in RSL of ~2.2 cm in Seattle, Washington, USA to a rise of ~14.44 cm in Crescent City, California, USA. In essence, both coasts of North America are affected by peripheral bulge subsidence which results in contemporary land subsidence ranging between a few tenths of to well over 1 mm/yr.

GIA related subsidence in Europe is less well explored than for North America. Much of this is due to the availability of high-quality, regional RSL datasets being available in North America for longer (e.g., Engelhart et al., 2011). Studies have been performed in Europe such as in in the Mediterranean (Vacchi et al., 2016) and in the UK with Gehrels et al. (2011) predicting a rate of ~1.13 mm/yr GIA-sourced subsidence in Devon, south-western UK by making use of sea-level

data dating back to 9000 cal. yr BP, and the GIA model from Bradley et al. (2009). This is reasonable when compared to data from Shennan et al. (2018) - which has RSL rise in the southeastern UK of up to 1.69 mm/yr (East Anglia), while the southwest UK, rates are closer to 0.6 mm/yr.

Studies examining changes in RSL closer to this project's study area include Goslin et al. (2015) which was performed in Brittany, France (Finistère region) and found almost all subsidence rates to be below 1 mm/yr (less than 0.7 mm/yr over the last 2000 years mostly due to GIA). However, they do remark that this should only be taken as an indicative value as this is based on few reliable data points. The study that covers this work's study area best is Leorri et al. (2012) which presented RSL data from Brittany, France, the Bay of Biscay, and Central/Southern parts of Portugal. This was intended to obtain estuarine samples in the Bay of Biscay as the region suffered from a lack of coverage by reliable data points. Results from this study show late Holocene millennial-scale rates of RSL rise ranging from approximately 0.3 to 0.7 mm/yr (from data younger than 7000 cal yr BP) across their total study region. They find a higher rates of sea-level rise in the northern parts of Europe as compared to southern parts and attribute this gradient to glacio-isostasy (as the dominant contributor). Despite the existence of Leorri et al. (2012) and other studies that have been performed there is a relative paucity of studies for the Atlantic coastline of Europe.

Observations of contemporary VLM via GPS have also been used to constrain and quantify the contribution of GIA to land subsidence in peripheral bulge regions. Often this is done in conjunction with RSL data such as in Karegar et al. (2016), which covers the Atlantic coast of North America. In this study they use data from continuous GPS stations and late Holocene RSL data (of the last 4000 years) and note the highest rates of peripheral bulge collapse of 1.3-1.5 mm/yr between ~39º N and ~37º N along the eastern coast of North America. They found discrepancies that cannot simply be explained by the shorter time series that are available from GPS stations, potentially due to such processes as groundwater extraction (e.g. between 38º N and 32.5º N). On the whole, they find significant agreement between GPS rates of VLM and RSL change seen in Holocene records but advise caution when using tide gauge data when studying sea-level rise in the region. This is positive as measurements of contemporary VLM from GPS stations are useful in identifying areas where GIA is not the dominant/only process at

work – other processes such as sediment loading/compaction, water extraction, etc. Yousefi et al. (2018) makes similar use of GPS stations in Pacific North America where the expected rates of RSL rise indicated by modeling based on sea-level curves should be similar. Yousefi et al. (2018), similarly to Karegar et al. (2016), uses GPS stations in part to help separate other processes affecting VLM rates, but also finds greater spatial variation across GPS stations than GIA outputs would suggest. GPS data have been used in Atlantic Europe in a similar capacity (e.g. Leorri et al., 2012) but as with GIA model predictions, are not fully implemented for the area. They do note significant differences in present-day vertical land motion once this rate is removed for Brest, France; the southern Bay of Biscay, Spain; and Lisbon, Portugal that does not directly fit with a direct north-south gradient for GIA-sourced VLM, or other unknown sources for present day VLM. As a caveat to the use of continuous GPS datasets for VLM, they generally exist for timeframes too short to provide the most precise results for future RSL change (Gehrels et al., 2011), thus making them more useful for supporting GIA modeling based on Holocene data. In this study, we make use of the data from Schumacher et al. (2018) to compare to results for the last 3-4 ka.

Our aims in this study are threefold: (i) extend previous work by considering a much larger suite of GIA (Earth and ice) model parameters; (ii) constrain these parameters and quantify model uncertainty using recently published RSL (García-Artola et al., 2018) and vertical land motion (Schumacher et al., 2018) data sets; and (iii) use the resulting model parameter estimates to perform a sea-level budget analysis for the study region to determine the relative importance of GIA for contemporary and future RSL changes.

2.2 Methods

2.2.1 RSL Data

Holocene sea-level data are taken from a recently published RSL database (García-Artola et al., 2018). The data are partitioned into 13 sites (Figure 2.1) and constrain Holocene RSL changes from northern France to southern Spain. These sites locations were preserved for individual site analysis, while also being grouped into 4 regions to investigate the possibility of lateral variations affecting RSL along this coastline. These four regions are the Northern French coast (sites 1-4), western French coast (sites 5-7), and north and west Iberian Peninsula coasts (sites 8-

10 and 11-13 respectively). The dataset is comprised of 340 data points, 214 of these are sea level index points (SLIPs) and 126 limiting data points. SLIPs indicate a specific range in space and time dictated by uncertainty in which sea level was located, while limiting data points, divided into marine limiting (ML) and terrestrial limiting (TL), indicate that sea level had to exist above (ML) or below (TL) them (considering height and time uncertainty).

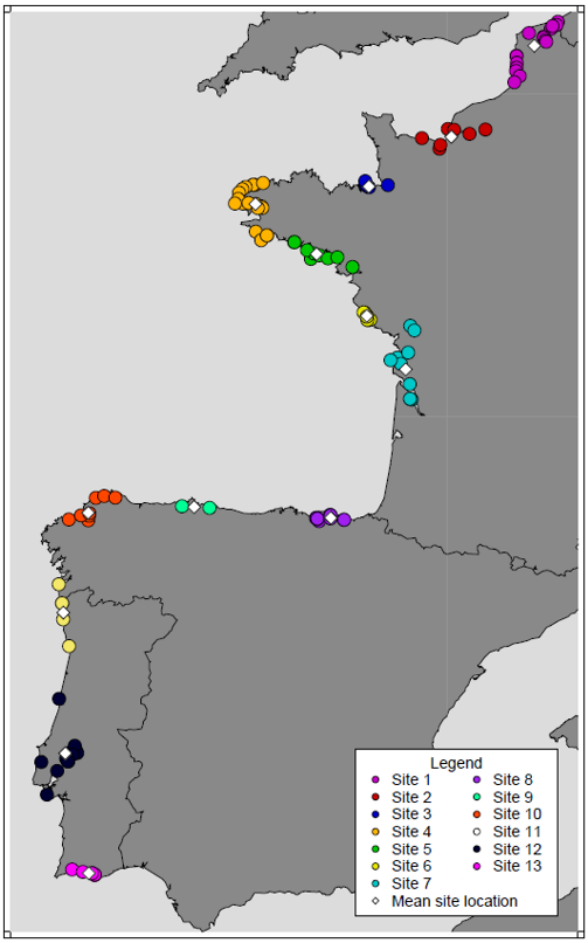

Figure 2.2. Map showing the spatial distribution of RSL data points across the study area. Mean site locations are denoted by white diamonds, whereas locations of individual datapoints (corresponding to SLIPs and limiting data points) are denoted by coloured circles with a different colour corresponding to each of the 13 site locations. Solid black lines denote national borders.

Figure 2.2 displays all data points on a single RSL-time plot. While this is inaccurate due to the considerable spatial variability in RSL across this region, we include it to provide a concise visual indication of the regional RSL signal. A more accurate presentation, with data partitioned into the 13 sites can be found in García-Artola et al. (2018), and in Section 2.3.1 below. It is important to note that some revisions were made to the original data set; specifically, the ages

were re-calibrated using the most recent calibration curves (Abrantes et al., 2005; Tisnérat-Laborde et al., 2010; etc. via CALIB Rev. 8) and some limiting data points were removed (25 ML and 4 TL) as they were redundant in terms of constraining RSL (e.g., Fig. S1). The older, early Holocene, RSL data begin around ~36 m below present sea level at 11.7 ka and show a rapid rise in RSL at a rate of approximately 6-6.2 m/kyr until ~6 ka when the rate significantly decelerates. The regional sea-level rise continues at a much slower rate (~1 m/kyr) through the mid-to-late Holocene. This temporal variation reflects a general slowdown in global ice sheet melting in the mid-Holocene (Lambeck et al., 2014). The slower but significant rate of RSL rise during the late Holocene (~6 ka to present) is characteristic of peripheral bulge regions, where GIA-associated land subsidence is a significant factor (Clark et al., 1978; Engelhart et al., 2009; Leorri et al., 2012).

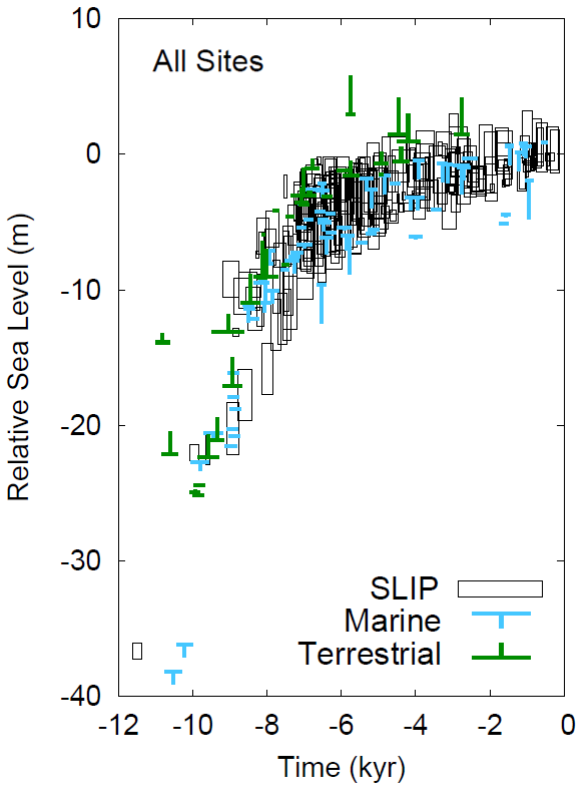

Figure 2.2. Reconstructed RSL for data locations shown in Fig. 2.1. Original dataset is from García-Artola et al. (2018), with ages recalibrated and some limiting data points removed (see text for details). The symbols are scaled to represent 1σ uncertainty ranges in time and RSL. Limiting data are plotted using T-shaped symbols for marine and terrestrial points (blue and green respectively) with the width of the horizontal line representing the ±1σ time uncertainty range and the vertical line representing a one-sided 1σ height uncertainty range (this is the emerging standard for plotting limiting data points; Khan et al., 2015).

The removal of redundant limiting data points was undertaken as their presence affects the data-model comparison via the misfit criterion (Eqn. 2; Section 2.2.4). Namely, the misfit criteria are normalised by the number of data points included, and thus redundant limiting data points bias the calculated misfit to a lower value. Therefore, a "cleaning" of the data was undertaken, the data for site 8 received the greatest amount of "cleaning" and so is presented in Figure S1, before and after the process, as an example.

In addition to removing some of the limiting data, a small number of SLIPs were also removed prior to the modelling analysis. Site 8 includes 12 SLIPs in the late Holocene which sit low relative to the contemporaneous ML data points. Furthermore, García-Artola et al. (2018) remark (p. 189) that these saltmarsh SLIPs are likely affected by sediment compaction due to land drainage for agricultural purposes. We have thus elected to omit all SLIP data points from site 8 and the three oldest SLIP data points from site 9 for similar reasons. Although these SLIPs were not considered in our data-model misfit calculations (Section 2.2.4), they are included in the relevant figures (using dashed lines) for completeness.

2.2.2 GPS Data

GPS data are taken from the global vertical land motion (VLM) data set presented by Schumacher et al. (2018). In said work, a global data set from the Nevada Geodetic Laboratory (NGL), and two regional datasets (one for Antarctica and one for Greenland) are synthesised before undergoing processing to attempt to remove vertical land motion (VLM) signals not related to GIA. VLM rates were estimated for the period 2005 to 2015 considering stations with at least 4 years of continuous data collection such that the calculated rates are not strongly influenced by shorter time scale processes. Post-processing was also undertaken to exclude stations with rates that lie outside a 3-sigma range defined using 13 global GIA forward model solutions chosen by the authors (resulting in 12.9% of sites being excluded). Additional post-processing included removing for the elastic VLM signal associated with mass changes in the ice sheets and glaciers as well as short-term polar motion during the period 2005 to 2015. Greenland and Antarctic ice sheets as well as globally-distributed glaciers and ice caps. We note that hydrological and atmospheric loading were not removed due to the large uncertainty in these signals. Further details can be found in Schumacher et al. (2018).

For geographic consistency with the RSL data, we considered only a subset of the Schumacher et al. (2018) data set from our study region. Specifically, only stations within 150 km of the Atlantic coastline. Other distances were considered (e.g., 50 km, 250 km) but 150 km was adopted as it provides a good balance between coastal proximity and sufficient density of data points along the shoreline (Figure 2.3). As expected, the VLM rates for this data set all reflect peripheral bulge subsidence.

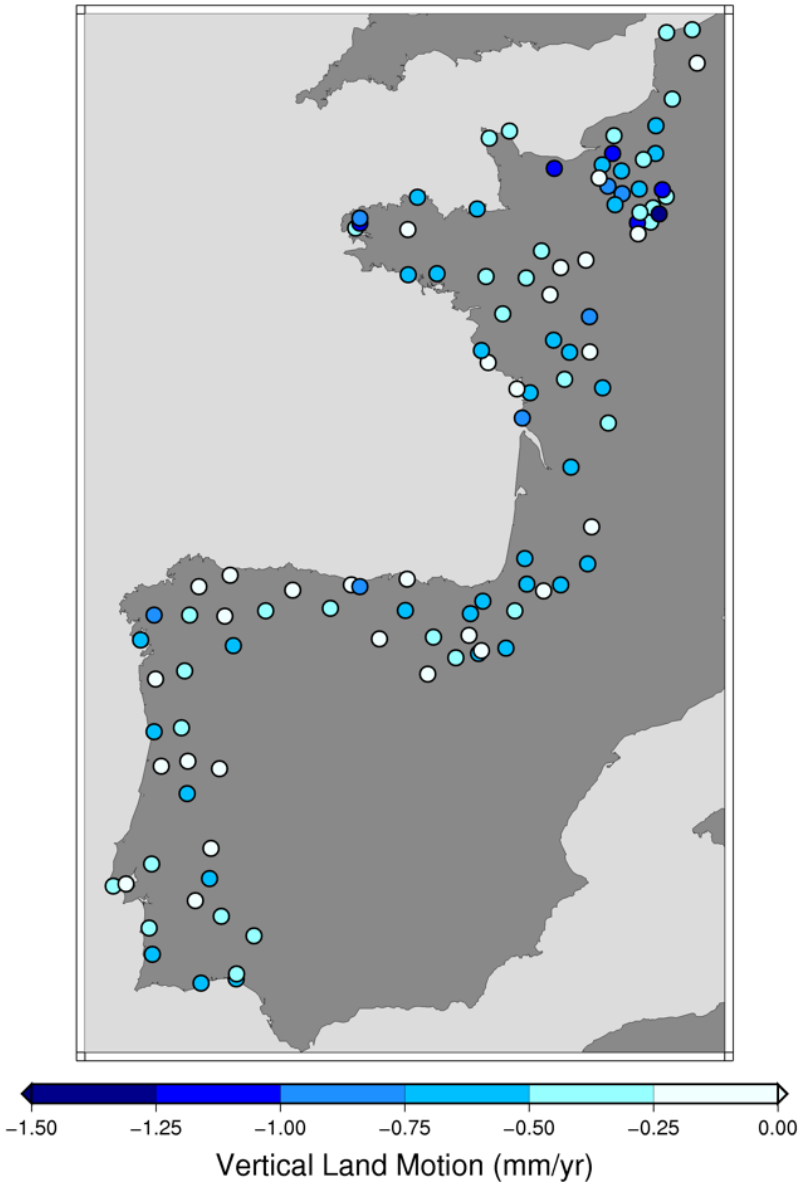

Figure 2.3. Vertical land motion at GPS stations within the study area taken from Schumacher et al. (2018). Stations depicted are those within 150 km of the coastline to better represent land motion relevant to the RSL sites shown in Fig. 2.1.

2.2.3 GIA Model

The GIA model used to calculate changes in sea level and VLM assumes a spherically symmetric Earth with a Maxwell rheology (Peltier, 1974). The depth-dependent viscosity structure is parameterised into three layers with the lithosphere as a highly viscous outer shell such that it acts as an elastic plate on GIA timescales. Multiple possible thicknesses for this outer shell were considered: 46, 71, 96 and 120 km. The model upper mantle extends from the base of the lithosphere to a depth of 671 km with uniform viscosity, and the model lower mantle extends from 671 km depth to the Core-Mantle boundary at 2885 km depth. The viscosity in the upper and lower mantle regions is assumed uniform with the following range of values considered: upper mantle viscosity (UMV) (0.05, 0.08, 0.1, 0.2, 0.3, 0.5, 0.8, 1.0, 2.0, 3.0, 5.0) $x10^{21}$ Pas and, lower mantle viscosity (LMV) (1, 2, 3, 5, 10, 20, 30, 50, 70, 90) $x10^{21}$ Pas. The elastic and density structure of the Earth model are parameterised with greater depth resolution (ranging from 1 km in the lithosphere to 30 km at the base of the lower mantle) with values taken from seismic constraints (Dziewonski and Anderson, 1981).

A primary input to the GIA model is a reconstruction of global ice thickness evolution during the Late Pleistocene (and Holocene). In total, seven ice loading histories were used in this study: ICE-6G(C) (Peltier et al., 2015), the global model developed by colleagues at the Australian National University (referred to as the ANU ice model; Lambeck et al., 2014 (see Hill et al., 2019 for key references)), and five models that are the same as ICE-6G(C) but include a different Fennoscandian ice sheet (FIS) component (Tarasov, 2013). These latter models were included to quantify the sensitivity of our results to the adopted FIS loading model.

An important component of any GIA model is the sea-level calculator. The code for this is based on the original sea-level equation presented in Farrell and Clark, (1976), with an algorithm described in Kendall et al. (2005) and incorporates the effects of GIA-induced changes to the Earth's rotation (Milne and Mitrovica, 1998; Mitrovica et al., 2005). As stated, the sea-level equation is part of the input and output of the GIA model as ocean-loading affects and responds to GIA processes, necessitating an iterative approach to solve the sea-level equation.

In total, approximately 3080 model runs were performed to sample the set of ice and Earth parameters defined above.

2.2.4 Estimating Model Parameters and Model Uncertainty

The quality of the data-model fit for each of the 3080 parameter sets considered was determined by calculating a misfit value. The optimal model parameter set, within the chosen parameter ranges, is that which results in the minimum data-model misfit. In the case of SLIPs, the misfit is computed by first determining the closest point on the model curve in height and time, and then calculating

$$\delta_{SLIP} = \frac{\sqrt{\sum_{n=1}^{N}((\Delta_{RSL,n})^2/\sigma_{RSL,n}^2+(\Delta_{t,n})^2/\sigma_{t,n}^2)}}{N} \qquad \text{(Eqn. 1)}$$

where $\Delta_{RSL,n}$ is the difference between observed and modeled RSL for the nth observation, while $\Delta_{t,n}$ is the equivalent for age, and $\sigma_{RSL,n}^2$ and $\sigma_{t,n}^2$ are the 1-σ observational uncertainty of the RSL and age data points, respectively. N is the total number of observational data for a given subregion. A simplified version of Eqn. 1, in which time differences were not considered, was used for the case of limiting RSL data given the one-sided height nature of this constraint

$$\delta_{Lim} = \frac{\sqrt{\sum_{n=1}^{N}((\Delta_{RSL,n})^2/\sigma_{RSL,n}^2)}}{N} \qquad \text{(Eqn. 2)}$$

In this case, no penalty is incurred if the model value is on the "correct" side of a given limiting point (notation as for Equation 1). Since limiting data are one-sided RSL constraints, when the misfit for an entire set of Earth parameters is calculated by means of Equation 3, the misfit is weighted at 0.5.

$$\delta_{Total} = \delta_{SLIP} + 0.5\delta_{Lim} \qquad \text{(Eqn. 3)}$$

The misfit for GPS-determined VLM rates was calculated using an equation that is equivalent to Eqn. 2 but where with the 'Δ' represents the difference between the observed and modelled VLM rate, and σ the uncertainty in the VLM observations.

Following Briggs and Tarasov (2013), the RSL data were weighted such that those with a relatively low density in time and/or space would have a greater weight in the misfit calculation. To account for spatial variations in data density, the RSL uncertainty is scaled to by the square root of the number of data points at a given site divided by the square root of the total number of data points for our entire study region. To account for variations in temporal data density at a

given site, the data were divided into four time bins (0-3, 3-6, 6-9, 9+ ka) and the age uncertainty was scaled by the square root of the number of data points in a given bin divided by the square root of the total number of data points at that site. While it is important to include this procedure, we can report that it did not have a significant impact on our results.

Model uncertainty is estimated using the Bayesian approach described in Love et al. (2016; their Section 2.3.2). Since a number of the requirements for accurate application of this approach are not met (Love et al., 2016), it provides only an estimate of the model uncertainty. For a given data set, the probability of a given model parameter set is given by

$$P(m|d) \propto P(d|m).P(m) \qquad \text{(Eqn. 4)}$$

where P(m|d) is the posterior probability of a specific model parameter vector (m) for a given data set (d), P(d|m) is the likelihood function and P(m) is the prior probability of a given parameter vector. For our application, we assume a uniform prior (P(m)) and define our likelihood function as

$$P(d|m) = e^{-\delta^2} \qquad \text{(Eqn. 5)}$$

where δ is the data-model misfit value for a specified model parameter set.

The posterior probabilities estimated from Equation 3 are normalized so that they sum to unity over the model ensemble. We adopt a 1-σ uncertainty threshold (i.e., 68.27%) to determine a sub-ensemble of the highest-probability model parameter sets. This sub-ensemble is then used to calculate a 1-σ range in model output for a given observable (e.g., RSL at model time steps). Therefore, the calculated model bounds generally reflect output from different model parameter sets within the determined (1-σ) sub-ensemble.

2.3 Results and Discussion

2.3.1 Model Parameter Estimation

Figure 2.4 depicts significant differences in data-model misfit values between global ice history models ANU and ICE-6G. Comparing results for the entirety of the data set (top two frames), the misfit results indicate that the ANU model generally produces better fits compared to ICE-6G for most Earth model parameter sets. Also, the optimal earth model parameter sets are not

compatible between the two ice models, with the ICE-6G model producing optimal fits for a region of viscosity space – high values of UMV (~3-5 × 10^{21} Pas) and low to average values of LMV (~2-5 × 10^{21} Pas) – that produces some of the poorest fits obtained with the ANU model. Model fits for different data sub-regions are also indicated in Fig. 2.4. These show that the quality of fit varies significantly between regions, with misfit values being highest for both models at sites 8-10. They also indicate that the ANU model produces better fits for the sub-regions with sites 1-4 and 8-10, with ICE-6G giving better results for regions with sites 5-7 and 11-13. Table 2.1 gives best-fitting sets of Earth parameters and corresponding misfit values for each data set considered in Fig. 2.4. We note that good fits for the ANU model (entire data set) are also produced for Earth models with high LMV values (~50-90 × 10^{21} Pas) which is consistent with the findings based on a global analysis of RSL observations (Lambeck et al., 2014).

Dataset	Best-Fitting ANU Ice Model & Earth Parameters	Misfit	Best-Fitting ICE-6G Ice Model & Earth Parameters	Misfit
All data	ANU 71-p2-1	0.407387	ICE-6G 120-5-3	1.280301
1-4	ANU 120-p2-50	0.184948	ICE-6G 46-5-2	0.432915
5-7	ANU 46-p08-1	0.271833	ICE-6G 96-p1-5	0.237692
8-10	ANU 46-p1-1	2.136292	ICE-6G 120-5-5	7.454214
11-13	ANU 46-p2-1	1.330928	ICE-6G 46-3-3	0.379806

Table 2.1. Summary of lowest misfits across ice models and data sets. Optimum Earth model parameters are given as a triplet: LT-UMV(x10^{21} Pas)-LMV(x10^{21} Pas).

Figure S2 shows misfit values for the regional ice history model FIS75954 as compared to the ICE-6G model and shows that changes to the FIS component of the model make relatively minor changes in data-model misfit (similar results were found using the other FIS model considered (Section 2.2.3). This reflects the fact that changes to the FIS component of the ice model have a relatively minor impact on the modelled RSL curves over the study region (see Fig. S3), with the largest differences being 2-3 m between FIS75954 and ICE-6G. Thus, we conclude that the differences apparent in Fig. 2.4 are dominated by differences in the barystatic component of the two global ice models. These differences, shown in Fig. S4 are significant, varying between ~3 m in the mid-Holocene to well over 10 m in the early Holocene. The improved fits for the ANU ice model for the majority of considered Earth viscosity models indicates that the barystatic

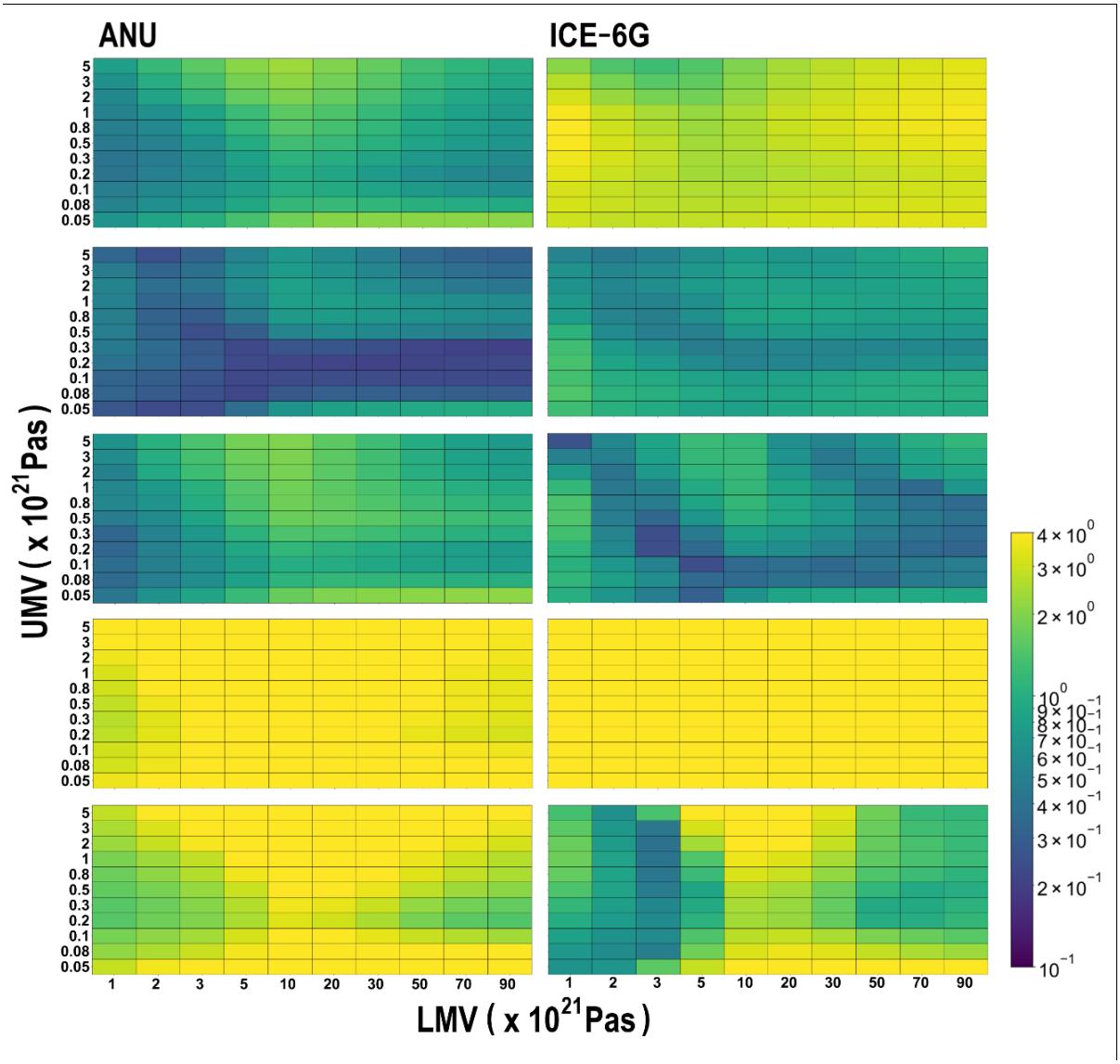

Figure 2.4. Data model misfit plots for the ANU (left column) and ICE-6G (right column) ice models. Top to Bottom: All data sites, sites 1-4, 5-7, 8-10, and 11-13, respectively. ANU results are for LT 71 km, ICE-6G are for an LT of 120 km (respective best fitting LT values).

function in the ANU model is more accurate. We return to this point below when estimating model uncertainty.

The misfit results (Fig. 2.4) are reflected in Fig. 2.5 which shows data-model comparisons using optimal Earth model parameters (based on the entire data set) at each site. All ice models fit the SLIP data well at most sites. However, as apparent in Fig. 2.4, the largest data-model misfits occur for regions 8-10 & 11-13. The optimal model curves based on the ICE-6G model (including FIS75954) sit below those for the ANU model during most of the Holocene. This is

counter intuitive given the differences between the barystatic component of these two global ice models (Fig. S4). This result reflects the large difference in the optimal viscosity model parameter sets (Fig. 2.4), particularly UMV, which results in markedly different RSL signatures in this region.

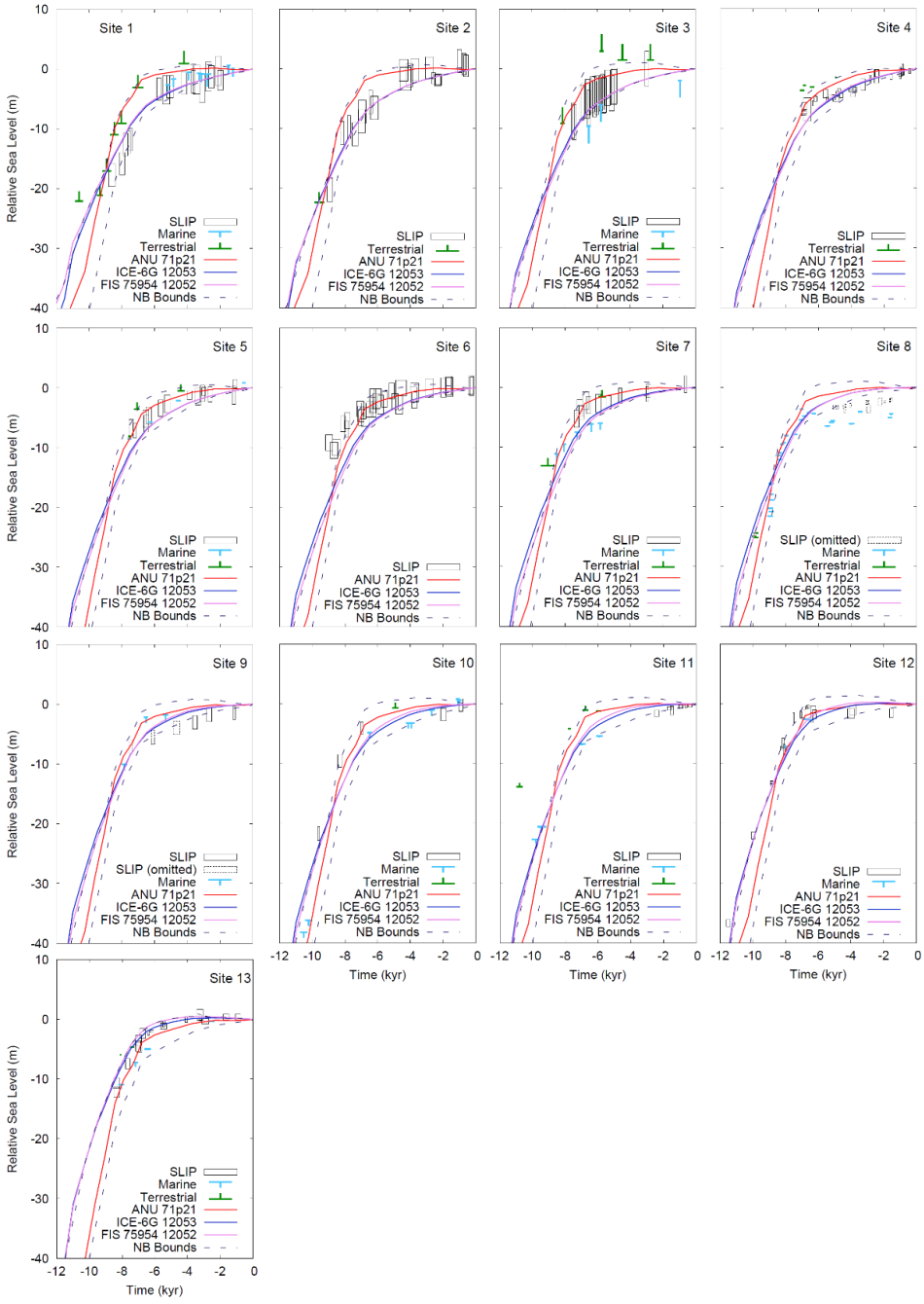

Figure 2.5. Data-model comparison by sites for entire RSL dataset and optimal Earth model parameters for entire data set for three ice models: ANU, ICE-6G, and FIS75954 (see key for details) and estimated 1-σ uncertainty margins.

Figures S5-S7 explore the data-model misfit for the three data-model subsets (TL, ML, and SLIPs, respectively). These figures show that the ANU model does a better job when considering the TL data but the ICE-6G model produces better results for the ML data at most locations. For the SLIPs, the misfit results are broadly similar between the two models. These three figures show that, although the ANU model best fits the entire dataset, the ICE-6G model can fit the data better for specific data types and sites. For instance, the ANU model often exhibits greater misfits for regions 8-10 and 11-13 for ML (Figure S6) and SLIP (Figure S7) data. While best-fitting Earth parameter sets based on ICE-6G may have lower misfits for specific data types at specific sites, when compared to those for the ANU model, the parameter sets that result in optimal fits are quite different for different data types, leading to a total misfit that is generally larger compared to that for the ANU model (Fig. 2.4, top frames).

Since the model sub-ensemble used to define model uncertainty is based on the misfit values (Section 2.2.4, Eqn. 5), preference of the RSL data for the ANU model is also evident in this aspect of the analysis. Of the entire ensemble based on three ice models (ANU, ICE-6G, FIS75954; 1320 runs in total), the estimated 1-σ sub-ensemble contains 203 sets of model output of which 201 were generated with the ANU model and 2 with the FIS75954 model. This sub-ensemble was used to define the model uncertainty range (dashed lines in Fig. 2.5) by picking the maximum and minimum RSL values from this sub-ensemble at each model time step. Since the model uncertainty range includes both global ice models (and thus quite different barystatic components), the 1-sigma range can be considered relatively conservative. Most of the data lie within the calculated uncertainty bounds, although there are some exceptions. For instance, site 6 includes two or three SLIPs that sit above the estimated upper bound around 8-9 ka, and site 10 includes one SLIP at ~10 ka that also sits at or above the upper bound. Model uncertainty bounds at site 12 miss two SLIPs, around 2, 8 and 12 ka. These relatively poor results for site 12 are reflected in the misfit results for this site. We note that all but one of the SLIPs at site 8 removed from the misfit calculation (Section 2.2.1) do not lie within the model uncertainty bounds, supporting our decision to treat these SLIPs as being inaccurate for the purpose of this analysis.

Figure 2.6 shows the same results as Fig. 2.4 but for the late Holocene (4ka to present) RSL data subset. Comparison of Figures 2.4 and 2.6 shows that the ANU-based misfit results change significantly less than those for the ICE-6G-based results. As expected, the misfit results for this

data subset are similar for each ice model, confirming the large impact of the barystatic signal when considering the complete data set. This result also confirms that the barystatic component of the ANU model is the more accurate of the two global models considered (since the misfit results were similar for each RSL data set). One striking feature of the misfit results is the sharp increase for sites 11-13 (lower frames) as LMV increases beyond 3-5 x 10^{21} Pas for most UMV values. Misfit and RSL curve analysis for sites within this region show site 13 is the primary source of this issue, with RSL curves either intersecting or missing a significant cluster of overlapping SLIPs as LMV values are varied.

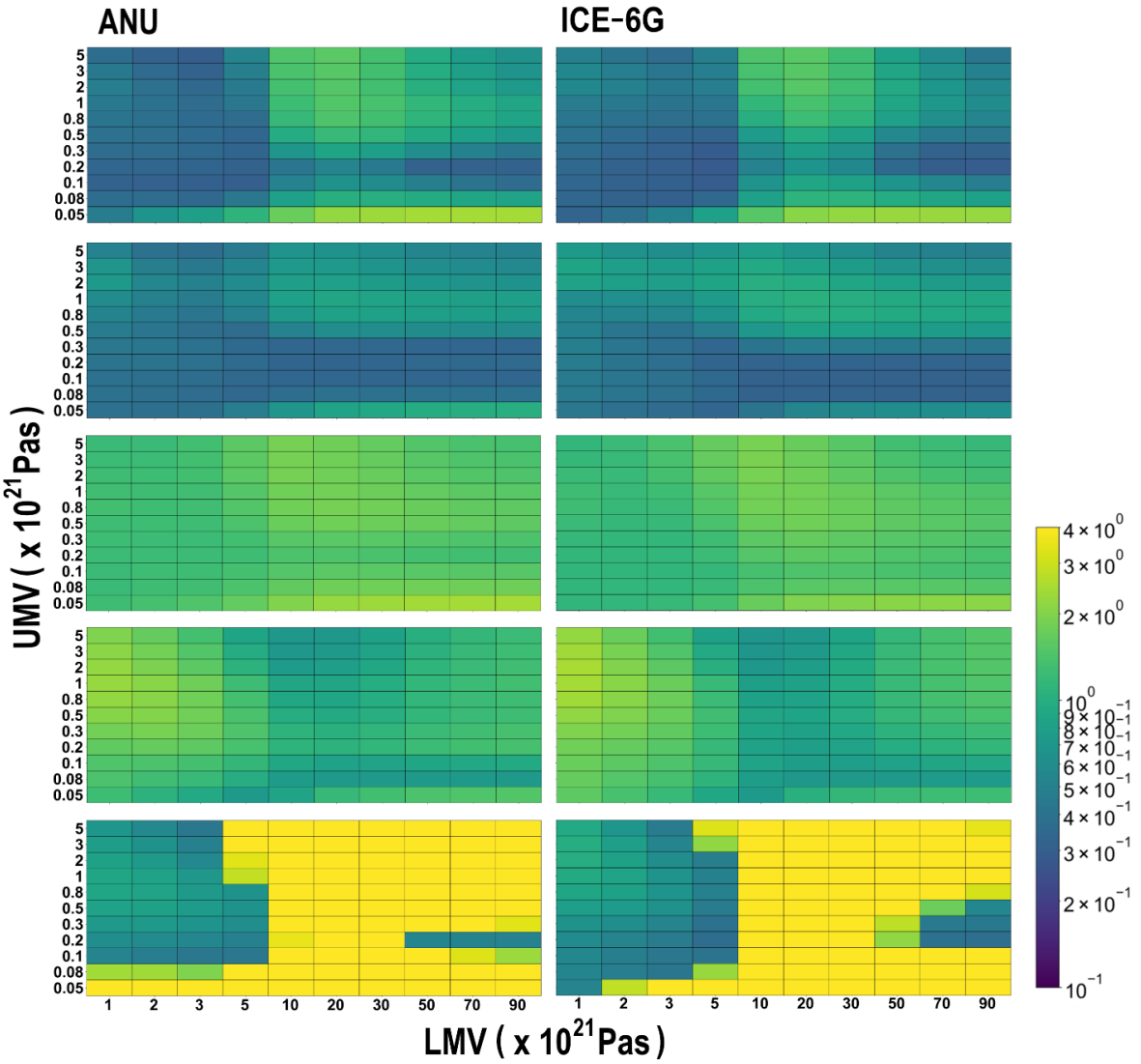

Figure 2.6. Data-model misfit plots calculated using only RSL data spanning the past 4 ka. Top to Bottom: All data sites, sites 1-4, 5-7, 8-10, and 11-13 respectively. ANU results are for LT 71 km, ICE-6G are for an LT of 120 km (respective best fitting LT values).

Data-model misfit analysis of VLM rates using the data set described in Section 2.2.2 yields the results in Figure 2.7. As for the misfit results using late Holocene RSL data (Fig. 2.6), the differences between misfit patterns for all considered ice histories (only those for ANU and ICE-6G shown) are small, indicating that that the modelled present-day vertical land motion signal is similar for each set of Earth model parameters. When comparing the VLM data misfits and those for late Holocene RSL data set (Fig. 2.6, top frames), the similarities are striking in terms of overall pattern and distribution of high and low misfit values, with the one exception being the cluster of higher misfits around UMV 0.8 x 10^{21} Pas and LMV 1 x 10^{21} Pas appearing in the GPS results about equally as strongly as the other two clusters of high misfit values that are apparent for both data sets. The quality of model fits to the GPS data set is apparent in Figure 2.8. The data-model residuals indicate that there is no apparent long-wavelength spatial gradient to within data precision, indicating no strong evidence for lateral variations in Earth viscosity structure. Over 90% of the optimal model results are within the observed 2-σ VLM range. The residuals indicated substantial scatter at short spatial scales which, most likely, reflects data uncertainty as well as signals associated with local processes (e.g., sediment compaction) and/or site effects (e.g., GPS receiver monumentation). The most spatially coherent residual is a cluster of slightly negative (<1σ) to quite negative (2-3σ) values in the northeastern-most quadrant of the study area (the French coastline along the English Channel), and what may be interpreted as an area of elevated positive values in Northwestern Spain. An alternative illustration of the data-model fits is provided in Fig. S8, which includes both data and model uncertainty (1σ). Overall, the model is compatible with the observations to within data and model uncertainty at long wavelengths but there are some significant residuals in localised areas, as noted above, that warrant further investigation. For future analyses, we provide model output of VLM for all GPS stations in France, Spain and Portugal in the Nevada Geodetic Laboratory catalogue (http://geodesy.unr.edu/NGLStationPages/gpsnetmap/GPSNetMap.html).

Since the misfit results for the late Holocene RSL and GPS data sets are broadly consistent, we generated results for these data sets combined (Fig. S9) to determine a more robust estimate of optimal Earth model parameters and uncertainty bounds. These results indicate that good fits can be obtained with a single set of EM parameters regardless of the chosen ice model. However,

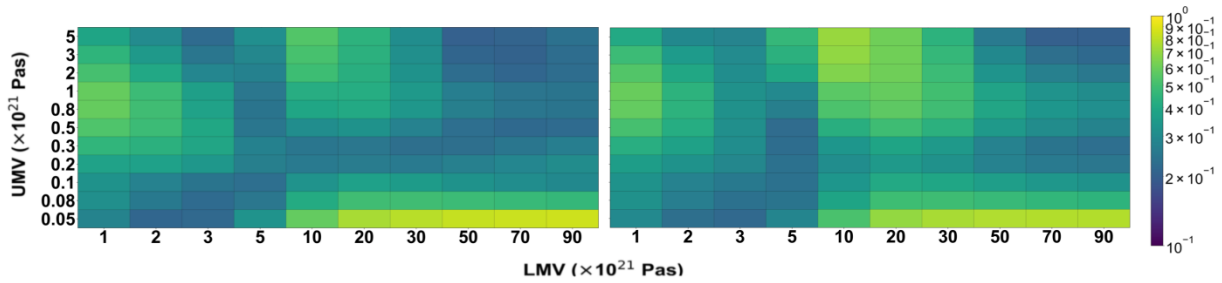

Figure 2.7. Data-model misfit plot for VLM data set described in Section 2.2.2. Left: ANU, right: ICE-6G.

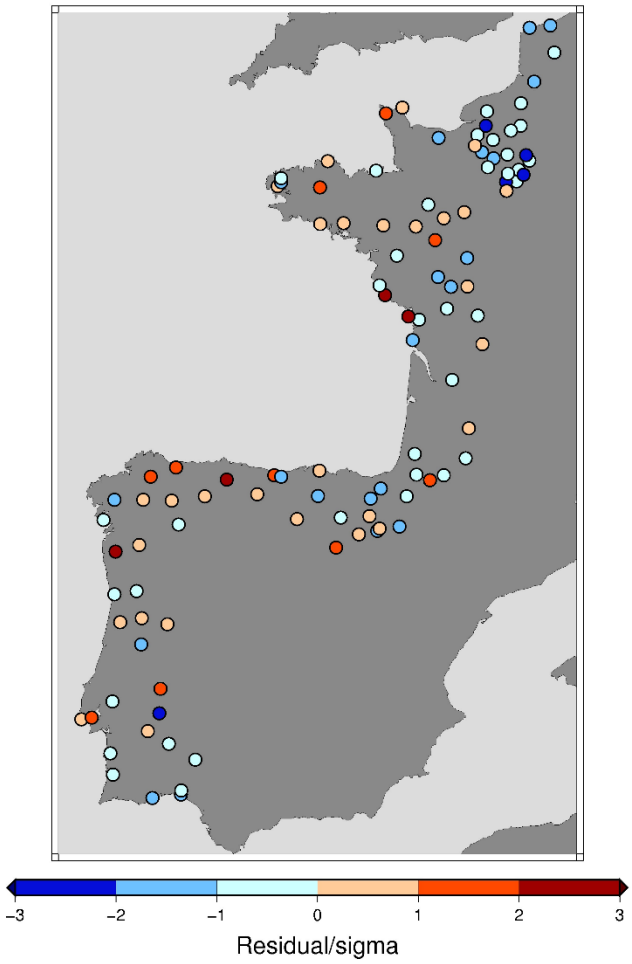

Figure 2.8. Data-model residuals (normalised by observational uncertainty) for model parameters (ANU/120-p3-50) that best fit the VLM data set described in Section 2.2.2.

there is clearly a considerable degree of non-uniqueness in defining an optimal model parameter set, as is often the case in GIA inversion problems. For example, the minimum misfit for the ANU model (1.6) was achieved with 120-p3-50, compared to a value of 1.48 with 46-5-70 for

the FIS75954 ice model. Compared to the results that considered only the complete set of RSL observations, in which the sub-ensemble of best-fitting models (203 out of 1320 parameter sets) was dominated by the ANU ice model, the uncertainty results based on late Holocene RSL data (4-0 ka) and VLM rates comprise a sub-ensemble of 108 parameter sets in which the three different ice models (ANU, ICE-6G, ICE-6G+FIS75954) appear approximately the same number times, indicating no significant bias related to the barystatic signal. The model uncertainty bounds for RSL during the late Holocene are shown with the optimal model curves and the RSL observations in Fig. S10. Generally, the model curves capture the data to within the estimated uncertainty ranges. However, there are a few exceptions, such as some low-lying SLIPs at sites 9, 11 and 12, and some anomalously high ML data points at sites 5 and 10. These data lying beyond model uncertainty bounds suggest that, for the case of SLIPs, compaction might be a greater issue than identified in previous studies (e.g., García-Artola et al., 2018).

2.3.2 General Discussion and Model Applications

2.3.2.1 Comparison to Previous Work

The results of Leorri et al. (2012) and García-Artola et al. (2018) share similarities and differences to the work presented here. The focus of these studies was more on the RSL observations with comparison to GIA model output being of secondary importance. For this reason, a much smaller number of model parameter sets were considered in these studies (7 in Leorri et al. (2012) and 1 in García-Artola et al. (2018)). Also, the RSL data set considered here (and in García-Artola et al., 2018), is considerably more extensive than that considered in Leorri et al. (2012). Our more in-depth modelling analysis supports these previous studies in that the observed RSL changes in this region are largely governed by peripheral bulge subsidence (glacio-isostasy) and continental levering (hydro-isostasy). The contributions of these GIA processes are plotted in Figure 2.9 for a model parameter set that fit well both the (total) RSL data set as well as the combined late Holocene RSL and GPS VLM data set (specifically: LT = 120 km, UMV = 3×10^{20} Pas, LMV = 5×10^{22} Pas). These model results indicate that RSL was lower in all parts of the study region at the model time step shown (6.8 ka), with a spatial variation of ~3.5 m along the coastal areas spanned by the RSL observations considered here. The rise in RSL since 6.8 ka was primarily driven by peripheral bulge subsidence in most areas,

although continental levering was considerable in some regions, such as northwestern France and Spain, and southern Portugal.

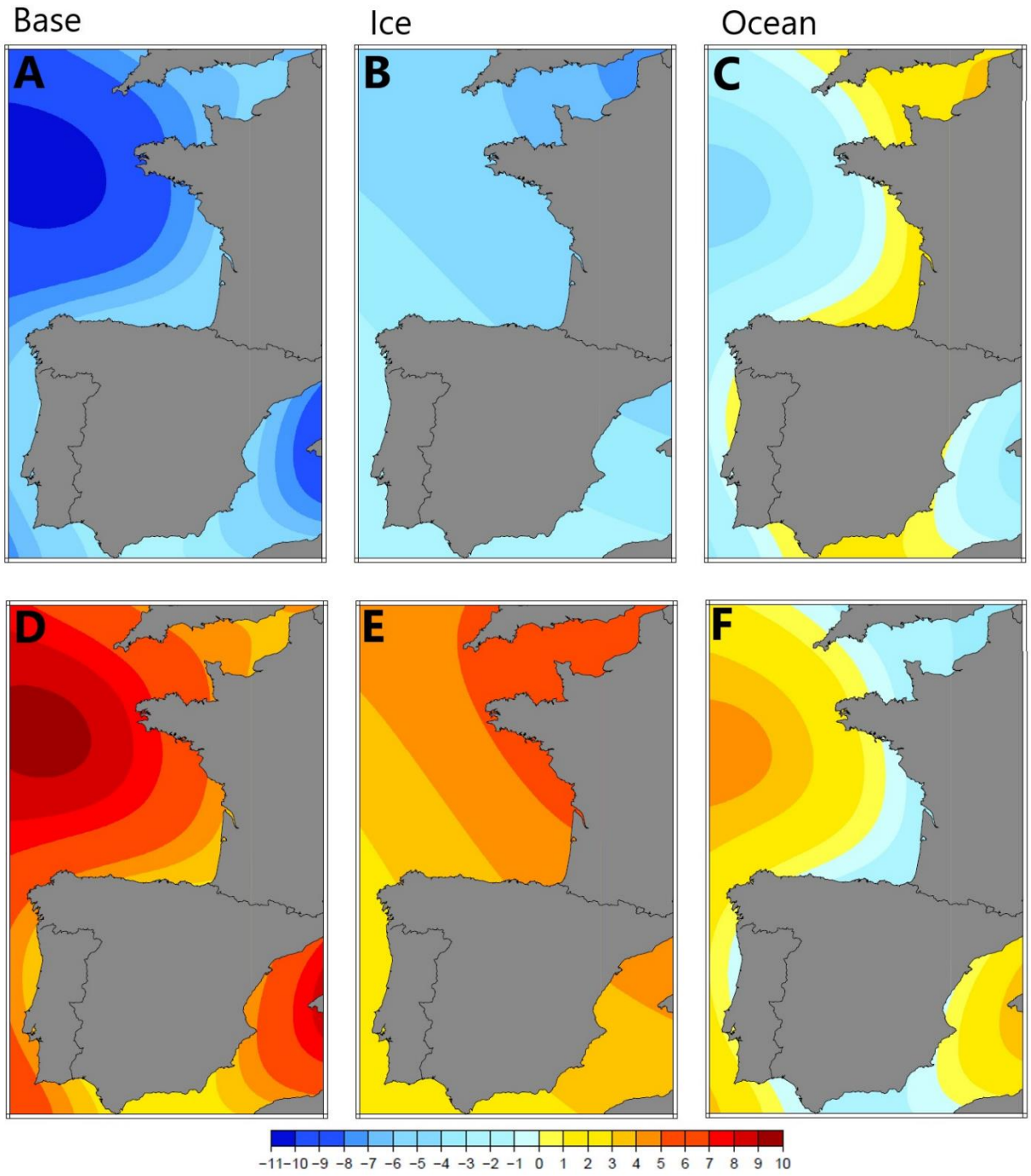

Figure 2.9. Model output of RSL (top row; A-C) and relative land height (bottom row; D-E) at 6.8 ka for the ANU ice model and Earth model parameter set 120-p3-50. Results are provided for the total signal (A, D) as well as that associated with only ice (B, E) or ocean (C, F) loading. Units are in metres.

The results in Fig. 2.9 vary as a function of model parameters but the general pattern and conclusions are robust. This is evident when comparing Fig. 2.9 to Fig. 4 in Leorri et al. (2012). The primary differences are a larger continental levering signal due to the lower LT (71 km) used in generating Fig. 4 of Leorri et al. (2012) and the orientation of the RSL gradient associated with glacio-isostasy, reflecting the different ice models being used in each case. As a third point of comparison, we include model output of these component signals for a parameter set that is favoured by the combined late Holocene and GPS VLM data set (Fig. S11; LT = 71 km, UMV = 5×10^{21} Pas, LMV = 7×10^{22} Pas). In this case, the significantly greater UMV (compared to Fig. 9 results) leads to much lower rates of deformation and therefore RSL changes that are approximately 50% of those shown in Fig. 2.9. These results demonstrate that variations in Earth model parameters to within the estimated parametric uncertainty can have a significant impact on the modelled RSL changes.

A key contribution of this work is the determination of model uncertainty. While it can be useful to define an 'optimal' parameter set for a given data set, it is more instructive and useful to define model bounds or uncertainty ranges to better illustrate the primary data-model misfits and highlight model shortcomings for future development and improvement. Furthermore, providing a range of model output that spans model uncertainty is more useful for end users seeking to include or remove the GIA signal as part of a different analysis (i.e., include it as part of a sea-level budget analysis (Section 2.3.2.2, below), or remove it to consider signals from other processes). In terms of fitting the RSL data, the primary challenge is to fit SLIPs that sit relatively high in the early Holocene while also fitting SLIPs that sit relatively low in the mid-to-late Holocene (Goslin et al., 2015; García-Artola et al., 2018). Consideration of model uncertainty is able to address many of the data-model misfits noted previously – specifically, high early Holocene RSL at sites 4, 10, 12 & 13 and low late Holocene RSL at sites 8, 9, & 11. We reiterate that at least some of these late Holocene data-model discrepancies are likely associated with the influence of sediment compaction due to anthropogenic activity (García-Artola et al., 2018). Even when considering model uncertainty (dashed lines in Fig. 2.5), there remain some misfits as noted in Section 2.3.1, but they are relatively minor.

In terms of reducing model uncertainty, our results suggest that improving constraints on the barystatic signal (as defined by the global ice history model) would be a logical first target as this

would lead to improved constraints on Earth model parameters. This aspect of the model is a primary contributor to the spread in the model uncertainty ranges. As noted above, our results indicate that the barystatic component of the ANU ice model is more accurate than that for ICE-6G. This is supported by the uncertainty analysis: (i) the ANU model is in the majority of accepted parameter sets and (ii) misfit results for the ANU model when late Holocene RSL and GPS VLM data sets were considered do not vary significantly. This conclusion aligns well with that of Goslin et al. (2015) who identified error in the barystatic signal as being a possible explanation for data-model misfits in northwestern France. They also suggested that uncertainty in the FIS could be a primary source of misfit. Our results based on the 5 different regional FIS models embedded in the global ICE-6G model indicate that variations in this aspect of the model play a relatively minor role.

2.3.2.2 Sea-Level Budget Analysis and Relative Importance of GIA in this Region

In this sub-section, we apply our new GIA model constraints in a sea-level budget analysis focusing on the latter half of the 20th century, specifically, the 40-yr period 1957 to 1997. This period was chosen as it pre-dates the satellite era and there are published constraints on the non-GIA signals that contribute to the observed sea-level response – changes in land ice (Greenland ice sheet, Antarctic ice sheet, glaciers), steric changes, and changes in terrestrial water storage (Frederikse et al., 2020). Only 10 tide gauge stations from our study region spanned the chosen time interval with relatively continuous data coverage (location map shown in Fig. S12). For these stations, we isolated the time series for each of the components signals, as provided by Frederikse et al. (2020), and performed the best linear unbiased estimation (BLUE) (Johnson, 2007) to find the rate and the accuracy of our estimation. This technique, which is based on the least squares techniques, ensures that the absolute, squared error (the difference between data and model) and the trace of the unknown's variance-covariance matrix are at a minimum. These criteria address the observation errors and the scattering of the measurements to find the best fit with the minimum error. In this technique, the observation's error is included in the inversion as weights, and the estimated rate is provided with uncertainty. These rates and associated uncertainties can be found in (Table 2.2). The amplitudes of the component signals is depicted visually in Fig. S13. The steric component dominates at all sites except at those adjacent to shallow seas (e.g., sites in Northern France adjacent to the English Channel). The uncertainty for

this component is also larger than that for all other component signals except for GIA. Glacier melting and GIA are the next two most important signals, with comparable amplitudes at most sites (although the mean GIA signal is more spatially variable, ranging from 0.3 to 0.7 mm/yr). Therefore, GIA is clearly an important contributor to 20th century RSL rise in this region and so should be included in estimates of past and future RSL change. Figure S14 provides a visual representation of the model output of the GIA contribution to present-day VLM using the Earth model parameters LT = 120 km, UMV = 0.3×10^{21} Pas, LMV = 50×10^{22} Pas for the ANU model. The rates seen are consistent with other rates seen in this work, with the largest signal being in and around Brest, France. The relative importance of GIA in this work compares favourably to Hammond et al. (2021), which found among other things that GIA was the most important factor driving VLM in Europe (and North America).

Our sea-level budget analysis is based on the following definition of the modelled rate of RSL (RRSL)

$$RRSL_{\mathrm{mod}} = RRSL_{steric} + RRSL_{AIS} + RRSL_{GrIS} + RRSL_{glaciers} + RRSL_{TWS} + RRSL_{GIA} \quad \text{(Eqn. 6)}$$

where each term represents the different component signals noted above. The difference between $RRSL_{mod}$ and the observed rate will reflect a bias in one or more of the component estimates or an unmodelled process (e.g., local VLM due to anthropogenic activity). The results in Table 2.2 indicate that the sea-level budget is not closed at all stations considered. Even if a more conservative 2σ uncertainty is adopted, the residual signal is non-zero at stations Dieppe, Le Havre, La Coruna I, Leixoes, and Cascais. Dieppe shows the largest residual, with an amplitude of ~4 mm/yr. Such a large amplitude suggests the contribution from an unmodelled VLM signal. However, the VLM rates of stations closest to Dieppe from the University of Nevada Geodetic Laboratory GPS data set (Blewitt et al., 2018) are insufficient to explain the amplitude of this residual (stations DIPP, SMEC, AMSL with values in mm/yr of 0.52 ± 0.89, -1.64 ± 0.71, and -1.64 ± 0.84, respectively). Furthermore, such a large signal would have been evident in our comparison of modelled and observed VLM rates (Section 2.3.1), although we note that these VLM data have been modified (Schumacher et al., 2018) for the purpose of comparison to GIA models.

Site	**Components**						**Sum of Components**	Measured Rate of RSL	Residual
	Glacier	TWS	Greenland Ice Sheet	Antarctic Ice Sheet	Steric	GIA			
Dunkerque (468)	0.340 ± 0.028	-0.195 ± 0.028	0.021 ± 0.002	0.053 ± 0.016	0.091 ± 0.042	0.362 ± 0.634	0.672 ± 0.636	1.692 ± 0.260	1.020 ± 0.688
Dieppe (474)	0.345 ± 0.028	-0.196 ± 0.028	0.023 ± 0.002	0.053 ± 0.016	0.062 ± 0.038	0.387 ± 0.515	0.675 ± 0.518	5.107 ± 0.199	4.432 ± 0.555
Le Havre (453)	0.351 ± 0.029	-0.194 ± 0.029	0.023 ± 0.002	0.053 ± 0.016	0.062 ±0.038	0.418 ± 0.482	0.714 ± 0.486	2.502 ± 0.167	1.788 ± 0.514
Brest (242)	0.371 ± 0.030	-0.212 ± 0.029	0.020 ± 0.002	0.056 ± 0.017	0.105 ± 0.061	0.686 ± 0.486	1.025 ± 0.492	1.191 ± 0.132	0.165 ± 0.509
St. Jean de Luz (469)	0.382 ± 0.032	-0.202 ± 0.028	0.052 ± 0.005	0.053 ± 0.016	0.688 ± 0.300	0.326 ± 0.414	1.299 ± 0.513	1.573 ±0.207	0.274 ± 0.553
La Coruna I (484)	0.400 ± 0.033	-0.210 ± 0.029	0.040 ± 0.004	0.057 ± 0.017	0.846 ± 0.364	0.539 ± 0.495	1.672 ± 0.616	2.947 ± 0.141	1.275 ± 0.632
Vigo (483)	0.405 ± 0.033	-0.215 ± 0.029	0.045 ± 0.004	0.057 ± 0.017	0.824 ± 0.340	0.484 ± 0.500	1.600 ± 0.606	2.416 ± 0.132	0.816 ± 0.620
Leixoes (791)	0.406 ± 0.033	-0.212 ± 0.029	0.051 ± 0.005	0.057 ± 0.017	0.902 ± 0.360	0.419 ± 0.519	1.622 ± 0.633	-0.449 ± 0.197	-2.071 ± 0.663
Cascais (52)	0.420 ± 0.035	-0.230 ± 0.0302	0.061 ± 0.006	0.057 ± 0.017	1.368 ± 0.613	0.417 ± 0.493	2.093 ± 0.789	0.289 ± 0.170	-1.803 ± 0.807
Lagos (162)	0.426 ± 0.036	-0.241 ± 0.030	0.072 ± 0.007	0.057 ± 0.017	0.950 ± 0.503	0.409 ± 0.505	1.672 ± 0.714	1.464 ± 0.216	-0.208 ± 0.746

Table 2.2. Summary of rates and associated uncertainties of all sites based on the set of Earth parameters that best fit ice history FIS 75954: 46 km, 5 ($x10^{21}$ Pas), 70 ($x10^{21}$ Pas). TWS = Terrestrial Water Storage. Units in mm/year.

2.4 Conclusions

Our results extend past work that considered RSL observations and the GIA contribution to the observed changes along the Atlantic coast of Europe (Leorri et al., 2012; Goslin et al., 2015; García-Artola et al., 2018). We present model results generated using seven ice history models and 440 Earth models (3080 GIA model parameter sets in total). With this broad range of parameter values, good quality fits to the Holocene RSL data were obtained. The best-fitting Earth model parameter sets varied considerably when two different global ice history models (ICE-6G and ANU) were applied, indicating the sensitivity of the Earth model parameter inferences to the barystatic component of the ice model. To reduce this dependency, a temporal subset of the RSL data was considered (past 4 ka) as well as observations of vertical land motion with non-GIA signals removed. Using these data sets, which are less dependent on the barystatic signal of the adopted ice model, provided a more robust inference of Earth model parameters. The results for these two data sets also indicated that the barystatic component of the ANU

model is more accurate than that of the ICE-6G model during the Holocene. Regarding the ice model, changing the Fennoscandian component made only minor changes to the model output.

Model uncertainty was determined using data-model misfit values and a nominally Bayesian approach to define a subset of parameter sets at a 1σ confidence level. When considering the model uncertainty, the majority of the Holocene RSL observations can be explained. There remain a small number of exceptions, particularly during the late Holocene in northern Spain, where a number of SLIPs fall below the model uncertainty range. These are most likely due to the compaction of the sediments containing the RSL indicators (Leorri et al., 2012; García-Artola et al., 2018). The majority of the VLM data set can also be explained when considering model uncertainty, with 8 of 107 failing to fit this criterion. However, there are some areas, notably northern France and Spain, where there are spatially coherent residuals, suggesting the importance of contemporary signals.

Our results support previous work in showing that GIA-related subsidence along the Atlantic coast of Europe is dominated by ice-loading (peripheral bulge) effects and that ocean loading is also important in some areas, such as northwestern France. The amplitude of these effects is strongly dependent on the chosen Earth model parameters. Using our subset of best-fitting parameter sets, we performed a sea-level budget analysis for the period 1957 to 1997 using data from 10 tide gauges in our study region. Using estimates of non-GIA signals from Frederikse et al. (2020), we find that the steric signal is the largest contributor at most of the considered tide gauge sites, with GIA and glacier signals the next largest. The steric and GIA signals dominate in terms of uncertainty at most sites. Of the 10 tide gauge stations considered, the budget was closed at five (to within 2σ uncertainty). The largest residual was found for station Dieppe in northern France, with an unexplained signal of 4.5 ± 0.5 mm/yr, suggesting a large unmodelled signal at this location (most likely related to vertical land motion). We provide GIA model output (including uncertainty) for rates of VLM at GPS stations in France, Portugal and Spain (included in the Nevada Geodetic Laboratory catalogue) and all tide gauge stations in our study region (included in the PSMSL catalogue).

Chapter 3: Conclusion

Using the HOLSEA dataset (from García-Artola et al., 2018) we have provided best-fitting sets of Earth parameters in furtherance of quantifying the GIA signal in Atlantic Europe. These results indicate that GIA remains an important factor when analysing present-day and future RSL projections, particularly in regions on the peripheral bulge of former ice sheets such as this as this subsidence adds to sea-level rise. These conclusions are corroborated by results gleaned from GPS rates from Schumacher et al. 2018. This effort has allowed for the partial success of our objective to use these resulting model parameter sets to perform a sea-level budget analysis. In this work, we have both supported conclusions made by previous studies performed in the northwestern Europe and identified potential gaps and inconsistencies in our understanding of the local Earth characteristics.

3.1 Summary of key results

In this section, I aim to summarise the main findings of Chapter 2 within a broader context to that provided in Section 2.4. Projected subsidence rates associated with the accepted model parameter values (at 1σ confidence) range from 0.67 mm/yr to over 2 mm/yr, with mean rates of VLM associated with GIA ranging between 0.3 and 0.7 mm/yr (corresponding to 3 to 7 cm over a period of 100 years). These are comparable to some GIA-related subsidence rates determined for North America, such as those for the west coast (Yousefi et al., 2018) with some reaching values of a few mm/yr, resulting in a contribution of GIA to sea-level rise being > 10 cm over the next century at some locations. In general, the rates of VLM associated with GIA can be substantially larger in North America. For instance, the component of rates of VLM attributable to GIA on the east coast of North America (Love et al., 2016) can be similar to our lower mean rates (e.g. ~0.3 mm/yr) but can range to values well above ours, such as projected sea-level rise due to GIA at some locations over the 21st century being up to a few decimeters (e.g. ~18 cm). This is not unexpected given that the Laurentide ice sheet was significantly larger than the Fennoscandian ice sheet at the last glacial maximum (Liakka and Loftverstrom, 2018).

With regards to our objective of constraining Earth viscosity structure, this study supports previous studies' findings that observed RSL changes in the region are largely governed by peripheral bulge subsidence (glacio-isostasy) and continental levering (hydro-isostasy), with

some differences related to uncertainty in constraining specific Earth model parameters (e.g., lithospheric thickness). Specifically, Leorri et al. (2012) predicts a relatively large continental levering signal due to favouring a 71 km thick lithosphere. They also predict a different pattern of glacio-isostasy due to their use of a different ice model. These differences are relatively minor and can be accommodated by uncertainty in the estimated parameter sets. Overall, we find that our results are in agreement with previous works in that we find that RSL rise since 6.8 ka is dominated by peripheral bulge subsidence. Our use of a much larger model parameter set and estimation of model uncertainty is a significant advance on previous work. This aspect has enabled us to identify suspect observations and determine that the barystatic component of the RSL signal, and not the regional glacio-isostatic signal, is the largest source of uncertainty.

Finally, in this work we find in constructing a rudimentary sea-level budget that the steric component dominates at all tide gauge sites that we could find for our chosen time period excepting those adjacent to shallow seas, with GIA and glacier melting being the next most important signals. GIA and the steric components were found to have the highest uncertainty. Comparing this to sea-level budgets on the east coast of North America, Love et al. (2016) has similar results insofar as the steric component is usually the largest component and with GIA and glaciers being the second largest, at least for middling to higher latitudes. They also found the greatest uncertainty was associated with the steric component with GIA (a component of VLM) having a relatively large uncertainty as well. Harvey et al. (2021) similarly has the stereodynamic component as the largest component with the GIA component approaching it in size in more northerly regions (for example Sewells Point).

3.2 Suggestions for future work

Despite finding no strong evidence for lateral variations in Earth viscosity structure, we believe that considering this additional model complexity would be worthwhile. Previous works have found that the addition of lateral Earth structure created better fitting results, albeit with significant uncertainty (Kuchar et al., 2019). Even considering model uncertainty, some of the RSL data could not be fit and so it is possible that a subtle long-wavelength associated with lateral viscosity variations could explain these remaining data-model residuals. Of course, if there is a significant signal associated with lateral Earth structure, this could have biased our inference of the radial (1D) viscosity parameters.

As noted elsewhere, GIA model uncertainty is relatively large and so further work should seek to reduce this uncertainty. This could be done by improving the barystatic component of this ice history model. As shown in our results, we found that the ANU model was the more accurate of the two ice models considered. With improvements in the quantity and quality of regional RSL data sets available to the GIA community (Khan et al., 2019), it is likely that better constrained ice sheet models will result. In terms of the glacio-isostatic signal, we found that the different FIS models made insignificant differences at our data locations. To improve upon sensitivity to this aspect of the GIA model, considering observations closer to the ice margin would be beneficial. In particular, considering RSL observations extending into Denmark, Germany, and possibly up into Fennoscandia with the goal of locating the hinge line (where subsidence caused by GIA turns to uplift) would be a logical extension of our analysis. Data from these regions have become available recently (for example, Rosentau et al., 2021).

Finally, given that in performing our examination of recent sea-level change through a sea-level budget analysis we found that half of the ten tide gauge sites have budgets that remain open, it would be potentially fruitful to perform additional analysis on sources of VLM as an explanation for residuals at these locations. In this work we did compare results to unfiltered rates of VLM as recorded at GPS stations near the tide gauge stations but this yielded no obvious solutions. It may be useful to incorporate additional ways of measuring VLM as a means of further exploring a possibly large and highly localised VLM signal. Interferometric synthetic aperture radar (InSAR) would be a good option for such an analysis as it can be used to produce a map of VLM rates with high spatial resolution. For example, Ohenhen et al. (2023) found the technique offered significant improvements when refining local and regional rates of sea-level rise (and thus inundation models) along the US Atlantic coast. Other works have found success using InSAR to measure subsidence in Southeast Asia (Hoyt et al., 2020), and creating inundation maps in Louisiana coastal wetlands (Oliver-Cabrera and Wdowsinski, 2016), to name a few locations. Satellite altimetry used in a similar manner to Martinez-Asensio, et al. (2019) would also be of interest, as their work made use of both remote satellite altimetry observations and GPS records to make more accurate present and future predictions of RSL change at Tropical Pacific Islands. These two methods of measuring VLM were implemented as the main source of uncertainty in projections seem to come from VLM estimates. This work does find discrepancies between rates of VLM as measured with GPS rates as these suggest larger RSL changes than

those projected using rates measured by altimetry or from GIA models. These would also be interesting to implement in Europe.

References

Abrantes, F., Lebreiro, S., Rodrigues, T., Gil, I., Bartels-Jonsdottir, H., Oliveira, P., Kissel, C., Grimalt, J. O., (2005). Shallow-marine sediment cores record climate variability and earthquake activity off Lisbon (Portugal) for the last 2000 years. Quaternary Science Reviews 24, 2477-2494.

Blewitt, G., Hammond, W. C., and Kreemer, C., (2018). Harnessing the GPS data explosion for interdisciplinary science, Eos, 99, https://doi.org/10.1029/2018EO104623. Published on 24 September 2018.

Bradley, S.L., Milne, G.A., Teferle, F.N., Bingley, R.M., Orliac, E.J., (2009). Glacial isostatic adjustment of the British Isles: new constraints from GPS measurements of crustal motion. Geophysical Journal International 178, 14–22. doi:10.1111/j.1365-246X.2008.04033.x.

Briggs, R.D., Tarasov, L. (2013). How to evaluate model-derived deglaciation chronologies: a case study using Antarctica, Quaternary Science Reviews, 63, 109-127, http://dx.doi.org/10.1016/j.quascirev.2012.11.021

CALIB rev. 8; Stuiver, M., and Reimer, P.J., 1993, Radiocarbon, 35, 215-230
Calib 8.20 <last accessed early 2021> http://calib.org/calib/calib.html

Church, J., P.U. Clark, A. Cazenave, J.M. Gregory, S. Jevrejeva, A. Levermann, M.A. Merrifield, G.A. Milne, R.S. Nerem, P.D. Nunn, A.J. Payne, W.T. Pfeffer, D. Stammer and A.S. Unnikrishnan (2013), Sea level change, Climate Change 2013: The Physical Science Basis. Contrib. of Working Group I to the Fifth Assessment Report Intergovernmental Panel on Climate Change. [Stocker, T.F., D. Qin, G.-K. Plattner, M. Tignor, S.K. Allen, J. Boschung, A. Nauels, Y. Xia, V. Bex and P.M. Midgley (eds.)]. Cambridge University Press, Cambridge, United Kingdom and New York, NY, USA.

Clark, J. A., W. E. Farrell, and W. Peltier (1978). Global changes in postglacial sea level: a numerical calculation, Quatern. Res., 9(3), 265–287, doi:10.1016/0033-5894(78)90033-9.

Conrad, C.P. (2013). The solid Earth's influence on sea level. Geological Society of America, 125, 1027-1052 doi: 10.1130/B30764.1

Davidson, N.C. (2014). How much wetland has the world lost? Long-term and recent trends in global wetland area. Marine and Freshwater Research, 65(10), 936-941 http://dx.doi.org/10.1071/MF14173

Davis, J.L., Mitrovica, J.X., (1996). Glacial isostatic adjustment and the anomalous tide gauge record of eastern North America, Nature, 379, 331–333.

Douglas, B. C. (2001). Sea level change in the era of the recording tide gauge. In B. C. Douglas, M. S. Kearney, & S. P. Leatherman (Eds.), Sea level rise, Int. Geophys, 75, 37–64. London. Academic Press. (chap. 3)

Dziewonski, A.M., Anderson, D.L., (1981). Preliminary reference Earth model. Physics of the Earth and Planetary Interiors, 25(4), 297-356 https://doi.org/10.1016/0031-9201(81)90046-7

Engelhart, S.E., Horton, B.P., Douglas, B.C., Peltier, W.R., Törnqvist, T.E, (2009). Spatial variability of late Holocene and 20th century sea-level rise along the Atlantic coast of the United States, Geology 37(12), 1115-1118 doi: 10.1130/G30360A.1

Engelhart, S.E., Horton, B.P., Douglas, B.C., (2011). Holocene relative sea-level changes and glacial isostatic adjustment of the U.S. Atlantic coast, Geology 39(8), 751-754 doi: 10.1130/G31857.1

Farrell W.E., Clark J.A. (1976). On Postglacial Sea Level. Geophysical Journal International, 46(3), 647–667, https://doi.org/10.1111/j.1365-246X.1976.tb01252.x

Fox-Kemper, B., H.T. Hewitt, C. Xiao, G. Aðalgeirsdóttir, S.S. Drijfhout, T.L. Edwards, N.R. Golledge, M. Hemer, R.E. Kopp, G. Krinner, A. Mix, D. Notz, S. Nowicki, I.S. Nurhati, L. Ruiz, J.-B. Sallée, A.B.A. Slangen, and Y. Yu, (2021). Ocean, Cryosphere and Sea Level Change. In Climate Change 2021: The Physical Science Basis. Contribution of Working Group I to the Sixth Assessment Report of the Intergovernmental Panel on Climate Change [Masson-Delmotte, V., P. Zhai, A. Pirani, S.L. Connors, C. Péan, S. Berger, N. Caud, Y. Chen, L. Goldfarb, M.I. Gomis, M. Huang, K. Leitzell, E. Lonnoy, J.B.R. Matthews, T.K. Maycock, T. Waterfield, O. Yelekçi, R. Yu, and B. Zhou (eds.)]. Cambridge University Press, Cambridge, United Kingdom and New York, NY, USA, pp. 1211–1362, doi:10.1017/9781009157896.011.

Frederikse, T., Landerer, F., Caron, L., Adhikari, S., Parkes, D., Humphrey, V.W., Dangendorf, S., Hogarth, P., Zanna, L., Cheng, L., Wu, Y-H., (2020). The causes of sea-level rise since 1900. Nature, 584, 393-397 https://doi.org/10.1038/s41586-020-2591-3

García-Artola, A., Stéphan, P., Cearreta, A., Kopp, R.E., Khan, N.S., Horton, B.P., (2018). Holocene sea-level database from the Atlantic coast of Europe. Quaternary Science Reviews, 196, 177-192 https://doi.org/10.1016/j.quascirev.2018.07.031

Gehrels, W.R., Dawson, D.A., Shaw, J., Marshall, W.A., (2011). Using Holocene relative sea-level data to inform future sea-level predictions: An example from southwest England. Global and planetary Change, 78, 116-126 doi:10.1016/j.gloplacha.2011.05.013

Gornitz,V. (2001). Impoundment, groundwater mining, and other hydrologic transformations: impacts on global sea level rise. In B.C. Douglas, M.S. Kearney, S.P. Leatherman (Eds.), Sea Level Rise: History and Consequences, Int. Geophys, 75, 97-119 (chap. 5) http://dx.doi.org.proxy.bib.uottawa.ca/10.1016/S0074-6142(01)80008-5

Goslin, J., Van Vliet-Lanoë, B., Spada, G., Bradley, S., Tarasov, L., Neill, S., Suanez, S., (2015). A new Holocene relative sea-level curve for western Brittany (France): Insights on isostatic dynamics along the Atlantic coasts of north-western Europe. Quaternary Science Reviews, 129, 341-365 https://doi.org/10.1016/j.aeolia.2022.100851

Hammond, W.C., Blewitt, G., Kreemer, C., Nerem, R.S., (2021). GPS Imaging of Global Vertical Land Motion for Studies of Sea Level Rise, Journal of Geophysical Research: Solid Earth, 126, e2021JB022355. https://doi.org/10.1029/2021JB022355

Harvey, K.M.: Handbook of sea-level research: framing research questions, in Handbook of Sea-level Research 1st ed., edited by: Shennan, I., Long, A.J., and Horton, B.P., John Wiley & Sons, West Sussex, UK, 66-82, https://doi.org/10.1002/9781118452547.ch25 2015.

Harvey, T.C., Hamlington, B.D., Frederikse, T., Nerem, R.S., Piecuch, C.G., Hammond, W.C., Blewitt, G., Thompson, P.R., Bekaert, D.P.S., Landerer, F.W., Reager, J.T., Kopp, R.E., Chandanpurkar, H., Fenty, I., Trossman, D., Walker, J.S., Boening, C., (2021). Ocean mass, stereodynamic effects, and vertical land motion largely explain US coast relative sea level rise. Communications Earth & Environment, 2(233) https://doi.org/10.1038/s43247-021-00300-w

Hill, A.M., Milne, G.A., Kuchar, J., Ranalli, G., (2019). Sensistivity of glacial adjustment to a partially molten layer at 410 km. Geophysical Journal International, 216, 1538-1548 doi: 10.1093/gji/ggy358

Holgate, S.J., Matthews, A., Woodworth, P.L., Rickards, L.J., Tamisiea, M.E., Bradshaw, E., Foden, P.R., Gordon, K.M., Jevrejeva, S., and Pugh, J., (2013). New Data Systems and Products at the Permanent Service for Mean Sea Level. Journal of Coastal Research: 29(3), 493-504. doi:10.2112/JCOASTRES-D-12-00175.1.

HOLSEA Initiative website https://www.holsea.org/

Hoyt, A.M., Chaussard, E., Seppalainen, S.S., Harvey, C.F., (2020). Widespread subsidence and carbon emissions across Southeast Asian peatlands. Nature Geosciences, 12, 435-440 https://doi.org/10.1038/s41561-020-0575-4

IPCC, 2023: Climate Change 2023: Synthesis Report. Contribution of Working Groups I, II and III to the Sixth Assessment Report of the Intergovernmental Panel on Climate Change [Core Writing Team, H. Lee and J. Romero (eds.)]. IPCC, Geneva, Switzerland, 35-115, doi: 10.59327/IPCC/AR6-9789291691647

IPCC, 2023: Summary for Policymakers. In: Climate Change 2023: Synthesis Report. A Report of the Intergovernmental Panel on Climate Change. Contribution of Working Groups I, II and III to the Sixth Assessment Report of the Intergovernmental Panel on Climate Change [Core Writing Team, H. Lee and J. Romero (eds.)]. IPCC, Geneva, Switzerland, 1-34, doi: 10.59327/IPCC/AR6-9789291691647.001

James, T.S., Gowan, E.J., Hutchinson, I., Clague, J.J., Barrie, J.V., Conway, K.W., (2009). Sea-level change and paleogeographic reconstructions for southern Vancouver Island, British Columbia, Canada, Quaternary Science Reviews, 28(13–14), 1200–1216. doi:10.1016/j.quascirev.2008.12.022

Johnson, R.A., Wichern, D.W.: Applied Multivariate Statistical Analysis, 6th Ed. Pearson Education Ltd. Upper Saddle River, New Jersey 07458, 2007

Karegar, M.A., Dixon, T.H., Engelhart, S.E., (2016). Subsidence along the Atlantic Coast of North America: Insights from GPS and late Holocene relative sea level data. Geophysical Reference Letters, 43, 3126-3133 doi:10.1002/2016GL068015.

Kendall RA, Mitrovica JX, Milne GA., (2005). On post-glacial sea level – II. Numerical formulation and comparative results on spherically symmetric models. Geophysical Journal International. 161(3), 679–706

Khan, N.S., Ashe, E., Shaw, T.A., Vacchi, M., Walker, J., Peltier, W.R., Kopp, R.E., Horton, B.P., (2015). Holocene Relative Sea-Level Changes from Near-, Intermediate-, and Far-Field Locations. Current Climate Change Report 1, 247-262, doi:10.1007/s40641-015-0029-z

Khan, N.S., Horton, B.P., Engelhart, S., Rovere, A., Vacchi, M., Ashe, E.L., Törnqvist, T.E., Dutton, A., Hijma, M.P., Shennan, I., and the HOLSEA working group, (2019). Inception of a global atlas of sea levels since the Last Glacial Maximum. Quaternary Science Reviews 220, 359-371 https://doi.org/10.1016/j.quascirev.2019.07.016

Kuchar, J., Milne, G., Latychev, K., (2019). The importance of lateral Earth structure for North American glacial isostatic adjustment. Earth and Planetary Science, 512, 236-245 https://doi.org/10.1016/j.epsl.2019.01.046

Lambeck, K., Smither, C., Johnston, P., (1998). Sea-level change, glacial rebound and mantle viscosity for northern Europe. Geophysical Journal International, 134, 102-144

Lambeck, K., Rouby, H., Purcell, A., Sun, Y., Sambridge, M. (2014). Sea level and global ice volumes for the Last Glacial Maximum to the Holocene. Earth, Atmospheric, and Planetary Sciences 111 (43), 15296-15303 https://doi.org/10.1073/pnas.1411762111

Leorri, E., Cearreta, A., Milne, G., (2012). Field observations and modelling of Holocene sea-level changes in the southern Bay of Biscay: implications for understanding current rates of relative sea-level change and vertical land motion along the Atlantic coast of SW Europe. Quaternary Science Reviews, 42, 59-73 doi:10.1016/j.quascirev.2012.03.014

Li, T., Wu, P., Wang, H., Steffen, H., Khan, N.S., Engelhart, S.E., Vacchi, M., Shaw, T.A., Peltier, W.R., Horton, B.P., (2020). Uncertainties of Glacial Isostatic Adjustment Model Predictions in North America Associated With 3D Structure. Geophysical Research Letters. 1-10 doi:10.1029/2020GL087944

Liakka, J., Lofverstrom, M., (2018). Arctic warming induced by the Laurentide Ice Sheet topography. Clim. Past., 14, 887-900

Love, R., Milne, G.A., Tarasov, L., Engelhart, S.E., Hijma, M.P., Latychev, K., Horton, B.P., Törnqvist, T.E., (2016). The contribution of glacial isostatic adjustment to projections of sea-level change along the Atlantic and Gulf coasts of North America. Earth's Future 4, 440-464. http://dx.doi.org/info:doi/10.1002/2016EF000363

Martinez-Asensio, A., Wöppelman, G., Ballu, V., Becker, M., Testut, L., Magnan, A.K., Duvat, V.K.E., (2019). Relative sea-level rise and the influence of vertical land motion at Tropical

Pacific Islands. Global and Planetary Change, 176, 132-143 https://doi.org/10.1016/j.gloplacha.2019.03.008

Maul, G.A., Duedall, I.W. (2019). Demography of Coastal Populations. In: Finkl, C.W., Makowski, C. (eds) Encyclopedia of Coastal Science. Encyclopedia of Earth Sciences Series. Springer, Cham. https://doi-org.proxy.bib.uottawa.ca/10.1007/978-3-319-93806-6_115

Milanković, M.: Kanon der Erdbestrahlung und seine Anwendung auf des Eiszeitenproblem. Special Publication 132, Section of Mathematical and Natural Sciences, 33, 633, 1941. Belgrade: Royal Serbian Academy of Sciences ('Canon of Insolation and the Ice Age Problem') (trans. Israel Program for the US Department of Commerce and the National Science Foundation, Washington 11 DC, 1969, and by Zavod za udzbenike i nastavna sredstva in cooperation with Muzej nauke itehnike Srpske akademije nauka i umetnosti, Beograd, 1998).

Milne, G.: Sea Level, in Coastal Environments and Global Change, 1st ed., edited by: Masselink, G. and Gehrels, R., John Wiley & Sons, West Sussex, UK, 28–51, https://doi.org/10.1002/9781119117261.ch2 2014.

Milne, G.A., Long, A.J., Bassett, S.E., (2005). Modelling Holocene relative sea-level observations from the Caribbean and South America. Quaternary Science Reviews 24, 1183-1202 doi:10.1016/j.quascirev.2004.10.005

Milne G A, Mitrovica J X. (1998). Postglacial sea-level change on a rotating Earth. Geophysical Journal International. 133(1), 1–19

Milne, G.A., & Shennan, I. (2013). Isostasy: Glaciation-Induced Sea-Level Change. Encyclopedia of Quaternary Science. 452-459. doi: 10.1016/B978-0-444-53643-3.00135-7.

Mitrovica, J.X., Milne, G.A., (2003). On post-glacial sea level: I. General theory. Geophysical Journal International. 154, 253-267

Mitrovica, J.X., Wahr J, Matsuyama I, Paulson A. (2005). The rotational stability of an ice-age Earth. Geophysical Journal International. 161(2), 491–506 https://doi.org/10.1111/j.1365-246X.2005.02609.x

Muhs, D.R., Simmons, K.R., Schumann, R.R., Groves, L.T., Mitrovica, J.X., Laurel, DA., (2012). Sea-level history during the Last Interglacial complex on San Nicolas Island California: implications for glacial isostatic adjustment processes, paleozoogeography and tectonics. Quaternary Science Reviews, 31, 1-25 doi:10.1016/j.quascirev.2012.01.010

Mulet, S., Rio, M-H., Etienne, H., Artana, C., Cancet, M., Dibarboure, G., Feng, H., Husson, R., Picot, N., Provost, C., Scrub, P.T. (2021). The new CNES-CLS18 global mean dynamic topography. European Geosciences Union 17, 615-649.

Nevada Geodetic Laboratory catalogue http://geodesy.unr.edu/NGLStationPages/gpsnetmap/GPSNetMap.html

Ohenhen, L.O., Shirzaei, M., Ojha, C., Kirwan, M.L., (2023). Hidden vulnerabilities of US Atlantic coast to sea-level rise due to vertical land motion. Nature Communications, 14(2038) https://doi.org/10.1038/s41467-023-37853-7

Oliver-Cabrera, T., Wdowsinski, S., (2016). InSAR-Based Mapping of Tidal Inundation Extent and Amplitude in Louisiana Coastal Wetlands. Remote Sensing, 8, 393 doi:10.3390/rs8050393

Peltier, W.R., (1974). The impulse response of a Maxwell Rheology Earth. Reviews of Geophysics, 12(4), 649-669 https://doi.org/10.1029/RG012i004p00649

Peltier, W.R., (1996). Mantle Viscosity and Ice-Age Ice Sheet Topography. Science 273(5280) 1359-1364

Peltier W.R. (1999). Global sea level rise and glacial isostatic adjustment. Global and Planetary Change, 20 (2–3), P. 93-123, ISSN 0921-8181. https://doi.org/10.1016/S0921-8181(98)00066-6

Peltier, W.R. (2004). Global Glacial Isostasy and the Surface of the Ice-Age Earth: The ICE-5G (VM2) Model and GRACE. Annual Review of Earth and Planetary Sciences, 32, 111-149 doi: 10.1146/annurev.earth.32.082503.144359

Peltier, W.R., Andrews, J.T., (1976). Glacial-Isostatic Adjustment – I The Forward Problem. Geophysical Journal International, 46(3), 605-646 https://doi.org/10.1111/j.1365-246X.1976.tb01251.x

Peltier, W. R., Argus, D.F., Drummond, R., (2015). Space geodesy constrains ice-age terminal deglaciation: The global ICE-6G C(VM5a) model. J. Geophys. Res. Solid Earth, 120, 450-487, https://doi.org/10.1002/2014JB011176

Rosentau, A., Klemann, V., Bennike, O., Steffen, H., Wehr, J., Latinović, M., Bagge, M., Ojala, A., Berglund, M., Becher, G.P., Schoning, K., Hansson, A., Nielsen, L., Clemmensen, L.B., Hede, M.U., Kroon, A., Pejrup, M., Sander, L., Stattegger, K., Schwarzer, K., Lampe, R., Lampe, M., Uścinowicz, S., Bitinas, A., Grudzinska, I., Vassiljev, J., Nirgi, T., Kublitskiy, Y., Subettor, D., (2021) A Holocene relative sea-level database for the Baltic Sea. Quaternary Science Review, 266, 107071 https://doi.org/10.1016/j.quascirev.2021.107071

Rovere, A., Stocchi, P. & Vacchi, M. (2016). Eustatic and Relative Sea Level Changes. Curr Clim Change Rep 2, 221–231 https://doi.org/10.1007/s40641-016-0045-7

Roy, K., Peltier, W.R., (2015). Glacial isostatic adjustment, relative sea level history and mantle viscosity: reconciling relative sea level model predictions for the U.S. East coast with geological constraints. Geophysical Journal International, 201, 1156-1181 doi: 10.1093/gji/ggv066

Ruddiman, WF.: Earth's Climate Past and Future. 3rd ed. W.H. Freeman and Company. New York. 2014

Schumacher, M., King, M.A., Rougier, J., Sha, Z., Khan, S.A., Bamber, J.L. (2018). A new global GPS data set for testing and improving modelled GIA uplift rates. Geophysical Journal International. 214, 2164-2176 doi: 10.1093/gji/ggy235

Shennan, I.: Handbook of sea-level research: framing research questions, in Handbook of Sea-level Research 1st ed., edited by: Shennan, I., Long, A.J., and Horton, B.P., John Wiley & Sons, West Sussex, UK, 3-25, https://doi.org/10.1002/9781118452547.ch2 2015.

Shennan, I., Bradley, S.L., Edwards, R., (2018). Relative sea-level changes and crustal movements in Britain and Ireland since the Last Glacial Maximum. Quaternary Science Reviews. 188, 143-159 https://doi.org/10.1016/j.quascirev.2018.03.031

Simpson, M.J.R., Milne, G.A., Huybrechts, P., Long, A.J., (2009). Calibrating a glaciological model of the Greenland ice sheet from the Last Glacial Maximum to present-day using field observations of relative sea level and ice extent, Quaternary Science Reviews, 28, 1631-1657 doi:10.1016/j.quascirev.2009.03.004

Slangen, A., C. Katsman, R. van de Wal, L. Vermeersen, and R. Riva, (2012). Towards regional projections of twenty-first century sea-level change based on IPCC SRES scenarios, Climate Dynamics, 38(5–6), 1191–1209, doi:10.1007/s00382-011-1057-6.

Stammer, D., Cazenave, A., Ponte, R.M., Tamisiea, M.E., (2013). Causes for Contemporary Regional Sea Level Changes. The Annual Review of Marine Science, 5, 21-46 doi: 10.1146/annurev-marine-121211-172406

Tarasov, L., (2013). GLAC-1b: a new data-constrained global deglacial ice sheet reconstruction from glaciological modelling and the challenge of missing ice, Geophys. Res. Abstr., 15, EGU2013–12342.

Tarasov, L., Dyke, A.S., Neal, R.M., Peltier, W.R., (2012). A data-calibrated distribution of deglacial chronologies for the North American ice complex from geological modeling, Earth and Planetary Science Letters, 315-316, 30-40 doi:10.1016/j.epsl.2011.09.010

Tisnérat-Laborde, N., Paterne, M., Métivier, B., Arnold, M., Yiou, P., Blamart, D., Raynaud, S., (2010). Variability of the northeast Atlantic sea surface D14C and marine reservoir age and the North Atlantic Oscillation (NAO). Quaternary Science Reviews (29), 2633-2646. http://dx.doi.org/10.1016/j.quascirev.2010.06.013

Vacchi, M., Marriner, N., Morhange, C., Spada, G., Fontana, A., Rovere, A., (2016). Multiproxy assessment of Holocene relative sea-level changes in the western Mediterranean: Sea-level variability and improvements in the definition of the isostatic signal, Earth-Science Reviews, 155, 172-197 http://dx.doi.org/10.1016/j.earscirev.2016.02.002

Vousdoukas, M.I., Mentaschi, L., Voukouvalas, E., Blanchi, A., Dottori, F., Feyen, L., (2018). Climatic and socioeconomic controls of future coastal flood risk in Europe. Nat. Clim. Change, 8(9), 776.

Wake, L., Milne, G., Leuliette, E., (2006). 20th Century sea-level change along the eastern US: Unravelling the contributions from steric changes, Greenland ice sheet mass balance and Late Pleistocene glacial loading, Earth and Planetary Science Letters, 250, 572-580 doi:10.1016/j.epsl.2006.08.006

Wessel, P. and W. H. F. Smith, (1991). Free software helps map and display data, EOS Trans. AGU, 72:41, 441-446 https://doi.org/10.1029/90EO00319

Whitehouse, Pippa L et al. (2019). Solid Earth change and the evolution of the Antarctic Ice Sheet, Nature communications 10(1), 1–14

Whitehouse P.L. (2018). Glacial isostatic adjustment modelling: historical perspectives, recent advances, and future directions. Earth Surf. Dynam., 6, 401–429. https://doi.org/10.5194/esurf-6-401-2018

Woodroffe, S.A., Long, W.J., Punwong, P., Selby, K., Bryant, C.L., Marchant, R., (2015). Radiocarbon dating of mangrove sediments to constrain Holocene relative sea-level change of Zanzibar in the southwest Indian Ocean, The Holocene, 25(2), 820-831 https://doi.org/10.1177/0959683615571422

Yokoyama, Y., Purcell, A., (2021). On the geophysical processes impacting palaeo-sea-level observations. Geoscience Letters, 8(13), https://doi.org/10.1186/s40562-021-00184-w

Yousefi, M., Milne, G.A., Love, R., Tarasov, L., (2018). Glacial isostatic adjustment along the Pacific coast of central North America. Quaternary Science Reviews. 193, 288-311 https://doi.org/10.1016/j.quascirev.2018.06.017

Appendix

Supplementary Figures

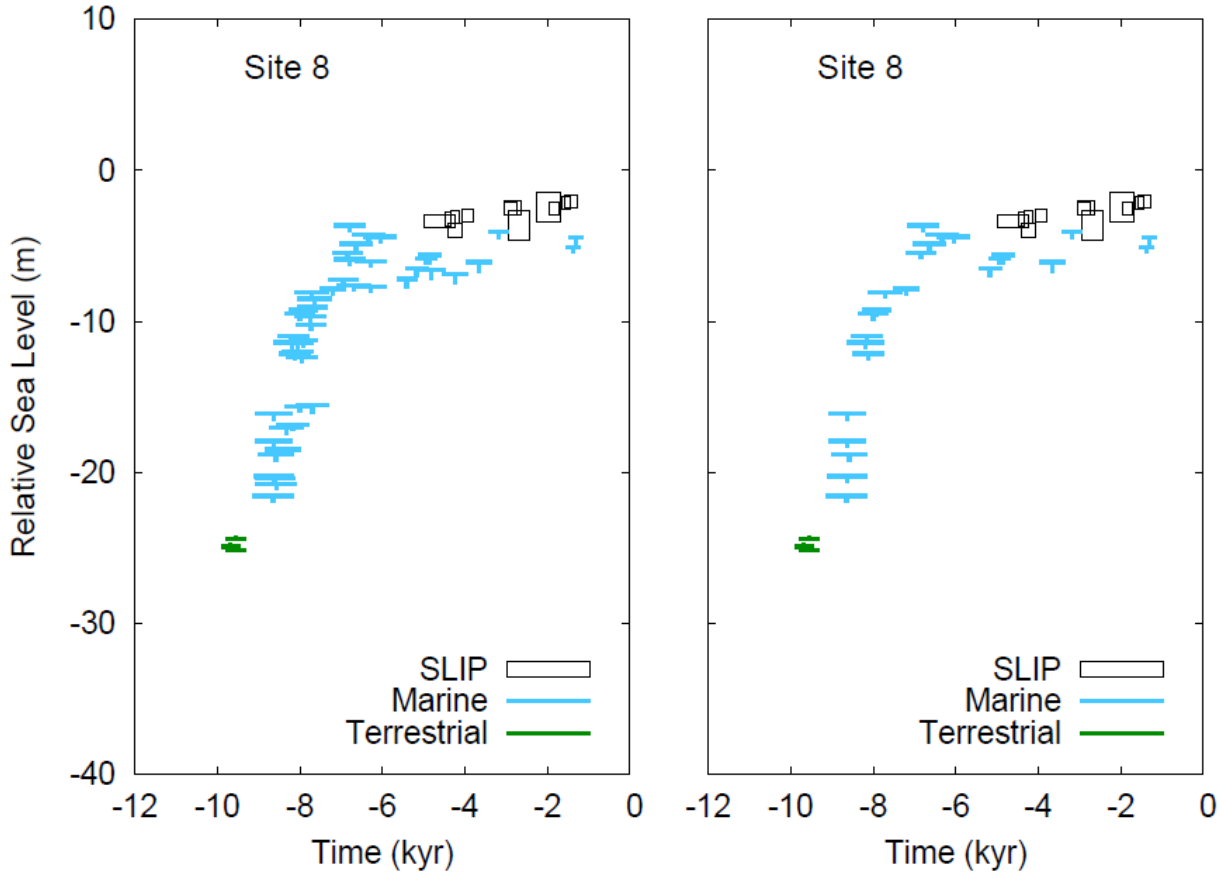

Figure S1. Comparison of full dataset (left plot) with dataset stripped of points deemed redundant (right plot). "Cleaning" of data points is based on a set of criteria as follows: data are removed for being significantly above or below the rest of the data.

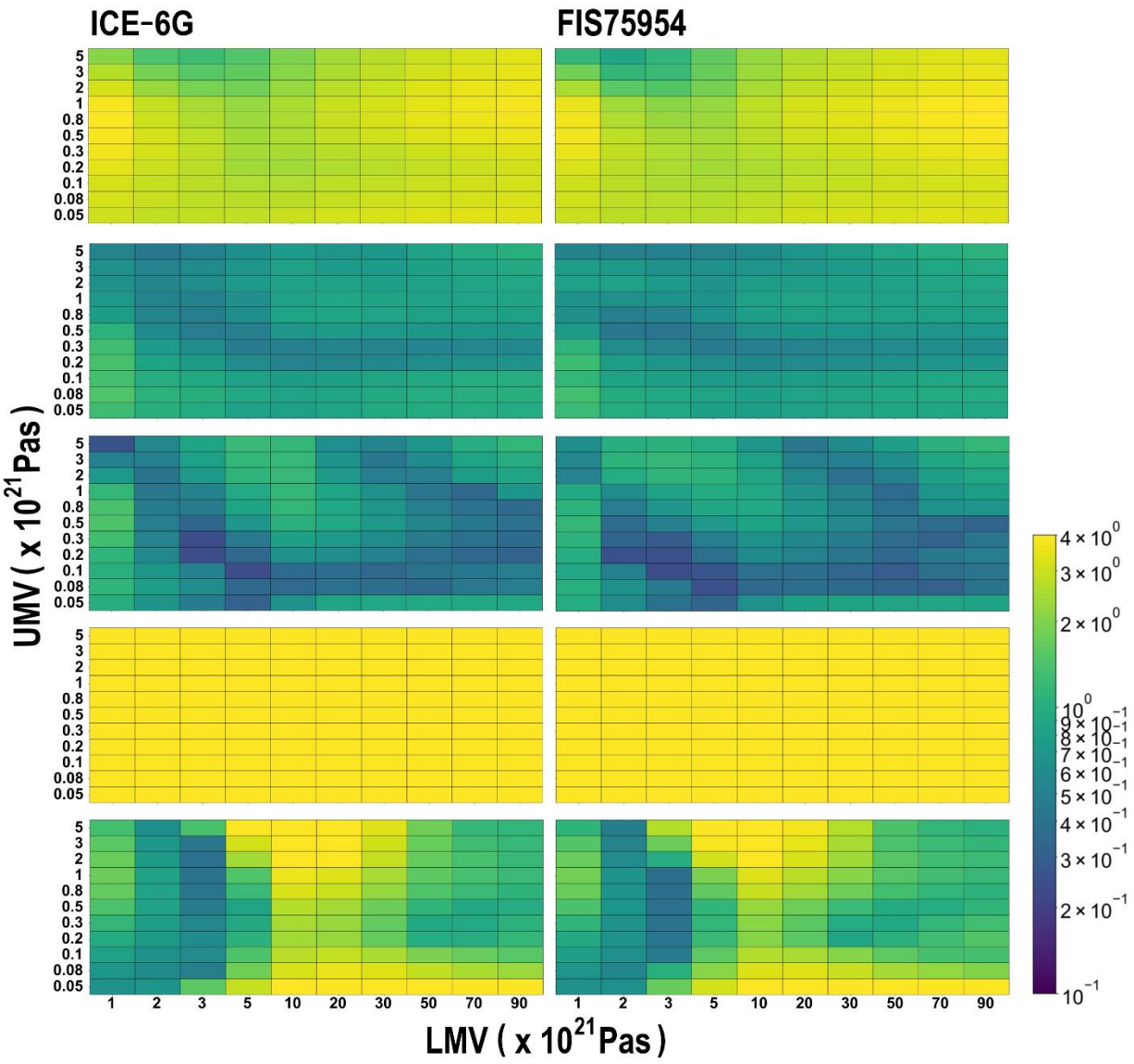

Figure S2. Data model misfit plots for the ICE-6G (left column) and FIS75954 (right column) ice models. Top to Bottom: All data sites, sites 1-4, 5-7, 8-10, and 11-13 respectively. All results based on an LT of 120.

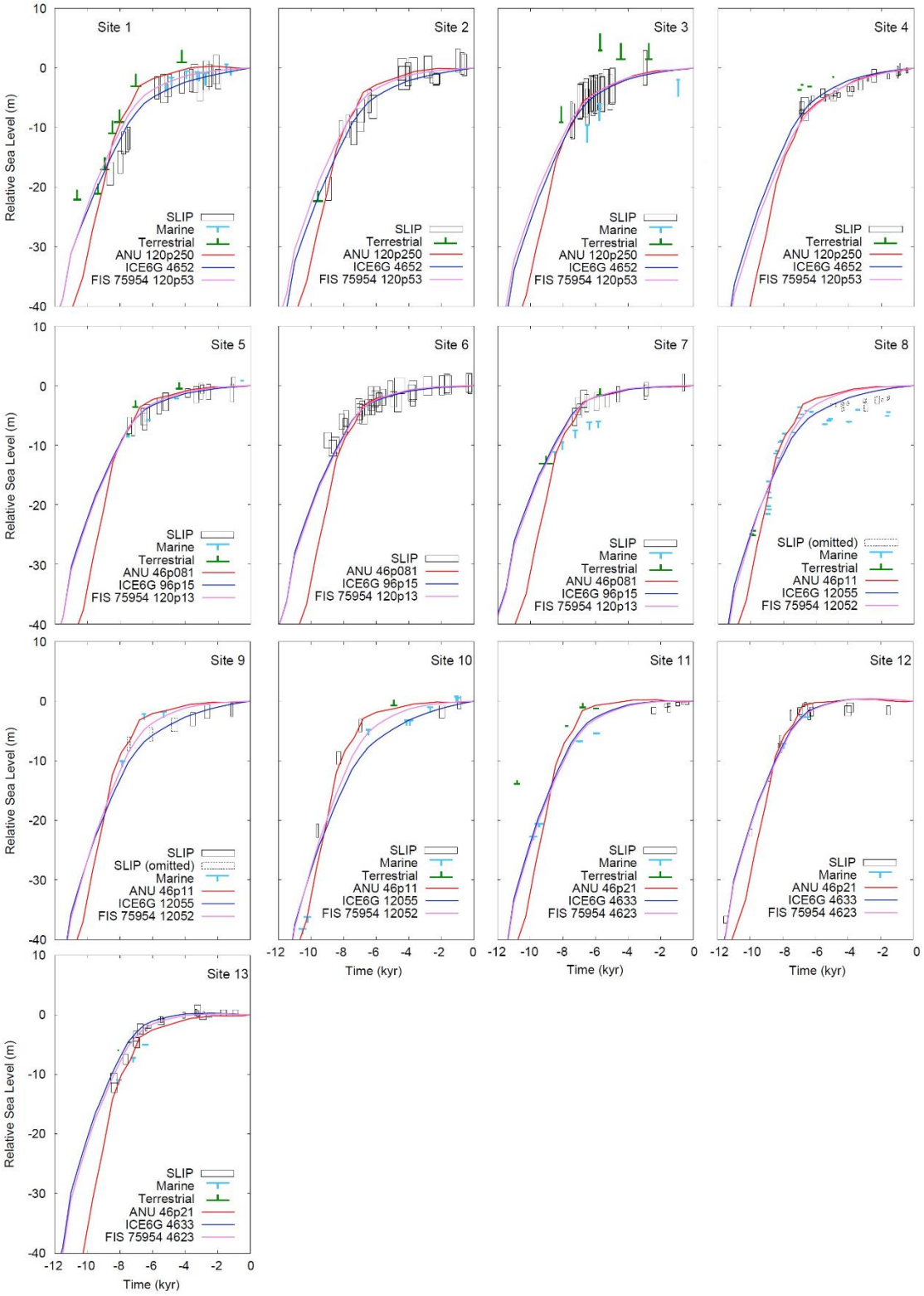

Figure S3. Data-model comparison by site for entire RSL dataset and regionally optimal Earth model parameters (the four regions encompassing respectively sites 1-4, 5-7, 8-10, 11-13) for three ice models: ANU, ICE-6G, and 75954 (see key for details).

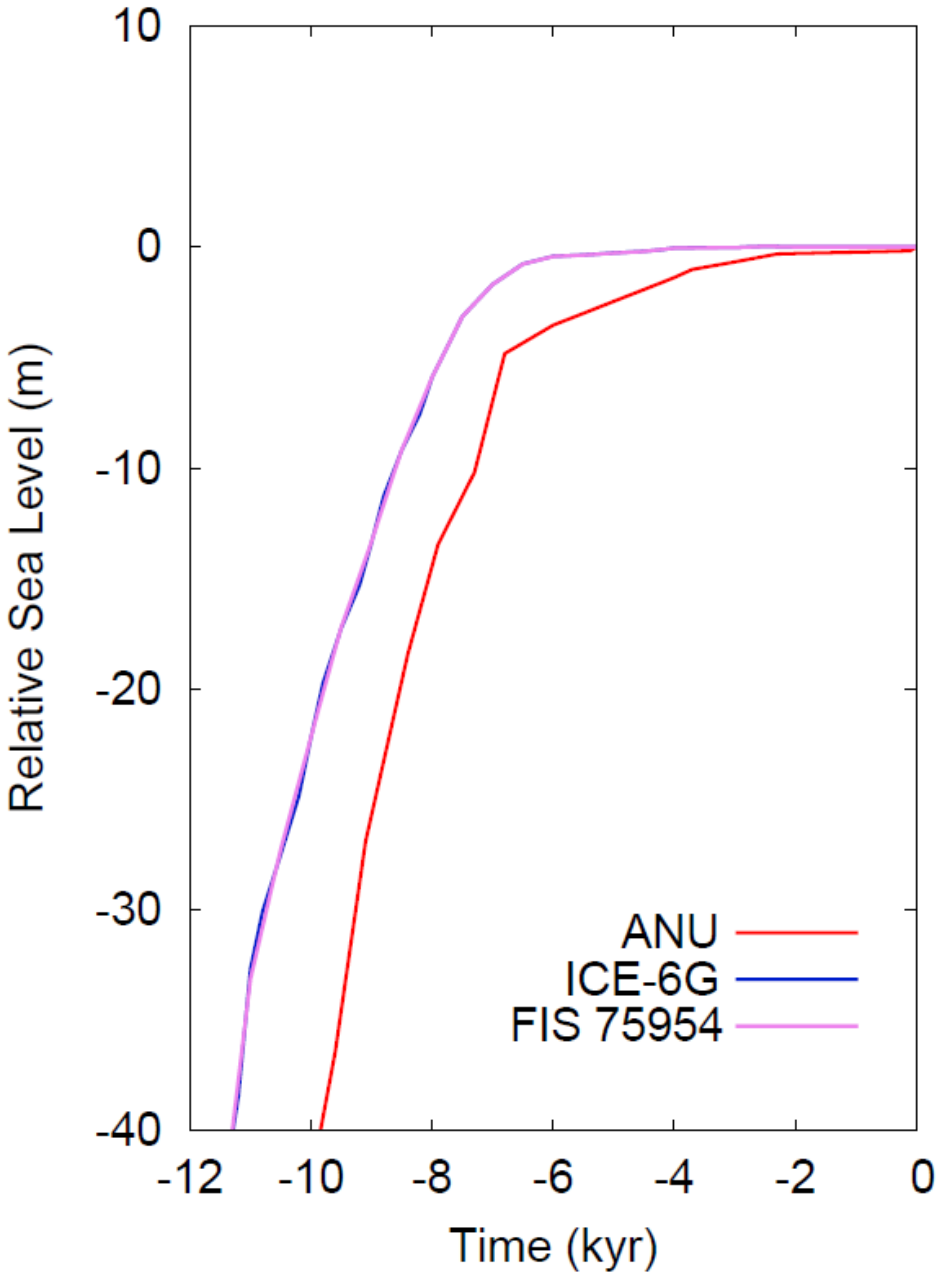

Figure S4. Data-model comparison for entire RSL dataset and barystatic component based on optimal Earth model parameters for entire data set for three ice models: ANU, ICE-6G, and 75954 (see key for details).

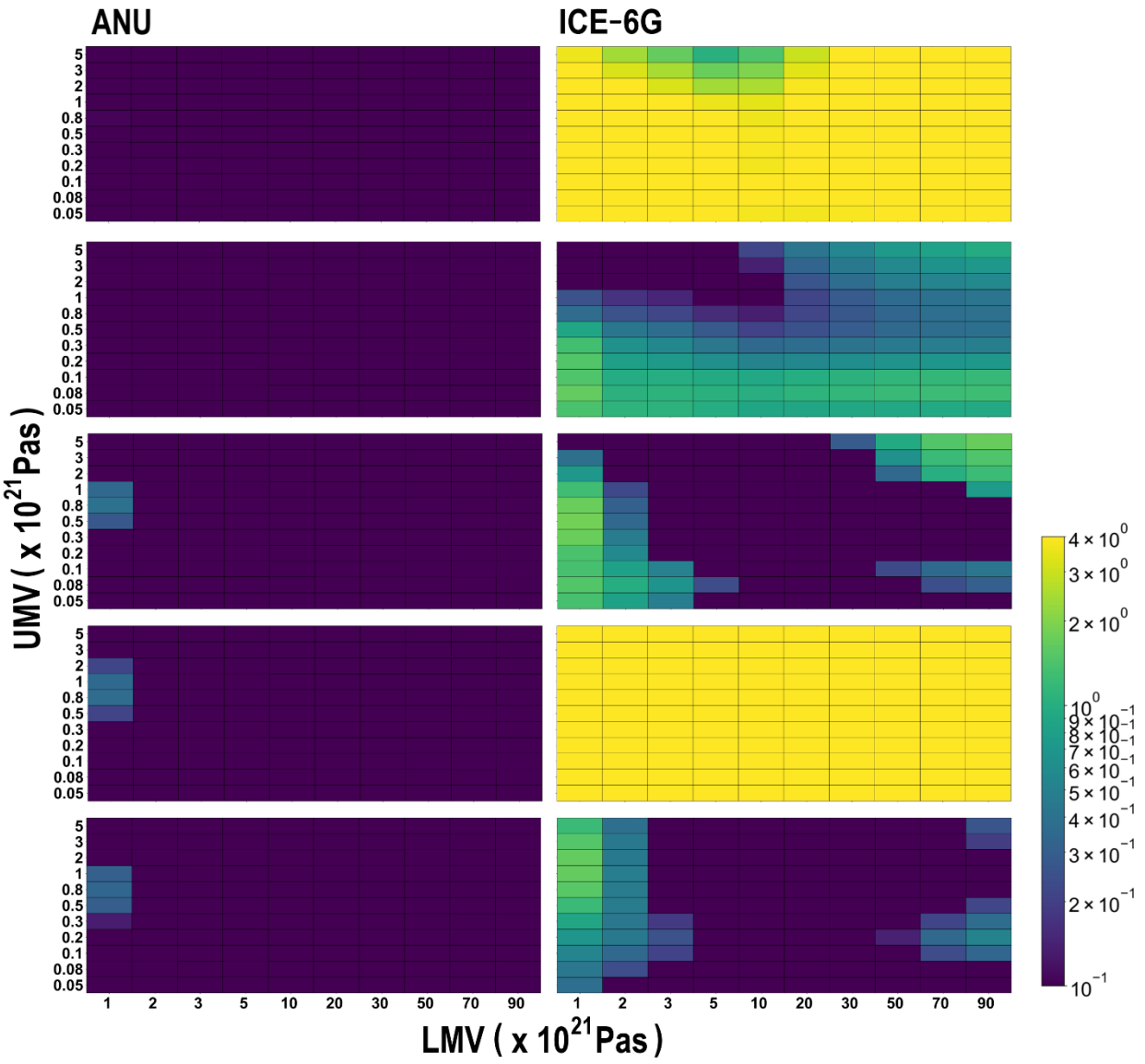

Figure S5. Data model misfit plots for full dataseries of TL data points for the ANU (left column) and ICE-6G (right column) ice models. Top to Bottom: All sites, sites 1-4, 5-7, 8-10, and 11-13, respectively. ANU results are for LT 71 km, ICE-6G are for an LT of 120 km (respective best fitting LT).

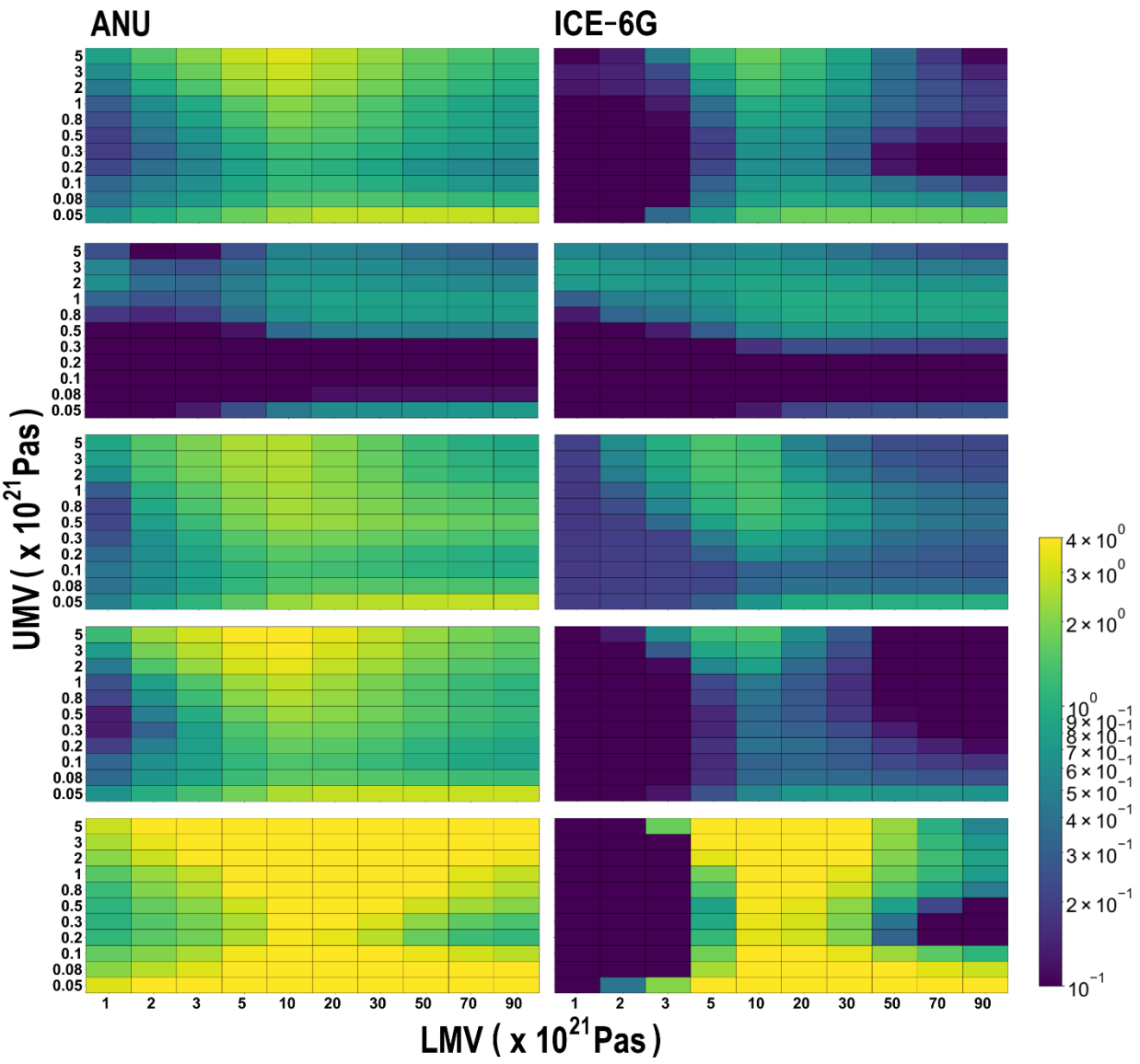

Figure S6. Data model misfit plots for full dataseries of ML data points for the ANU (left column) and ICE-6G (right column) ice models. Top to Bottom: All sites, sites 1-4, 5-7, 8-10, and 11-13, respectively. ANU results are for LT 71 km, ICE-6G are for an LT of 120 km (respective best fitting LT).

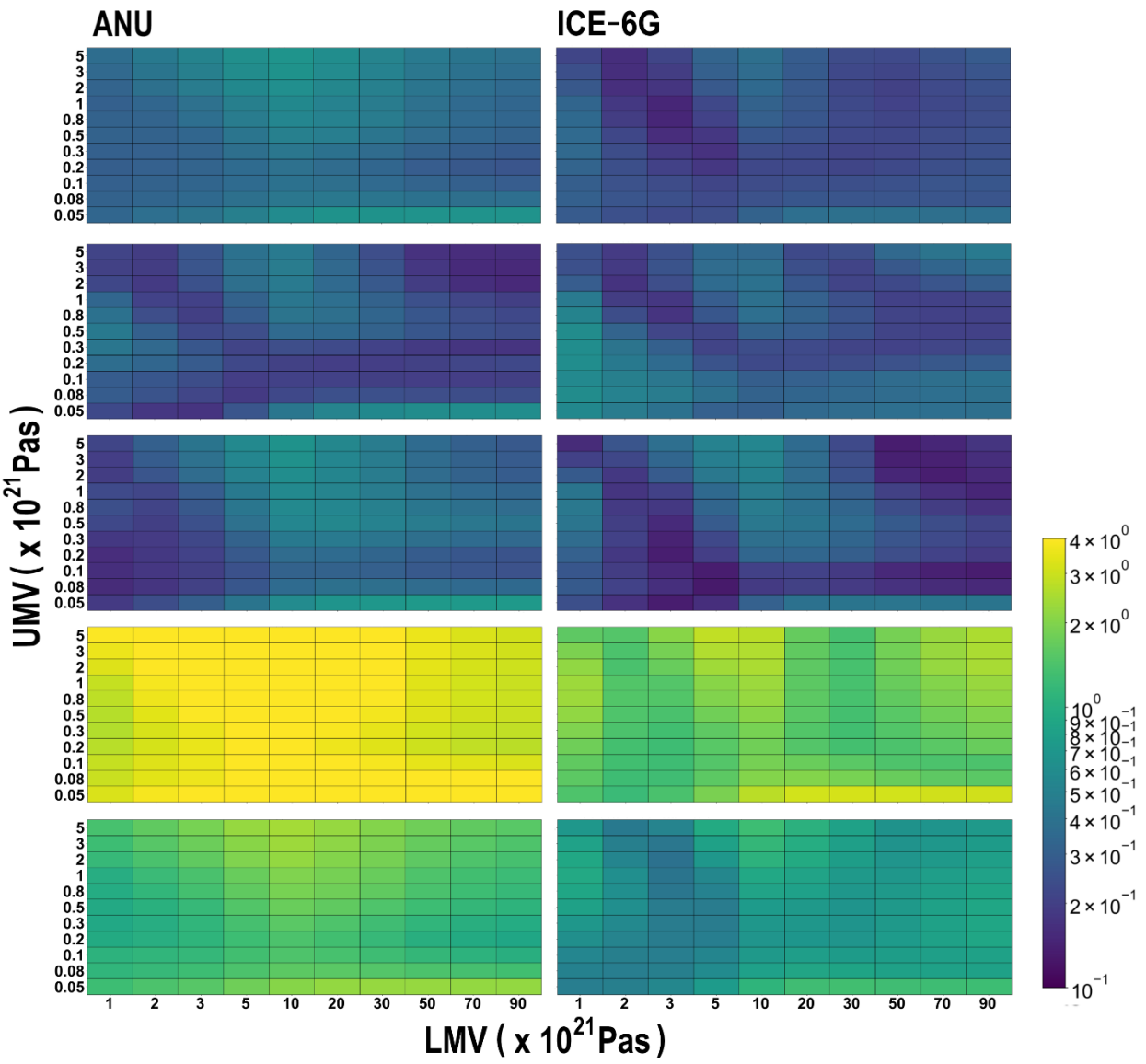

Figure S7. Data model misfit plots for full dataseries of SLIP data points for the ANU (left column) and ICE-6G (right column) ice models. Top to Bottom: All sites, sites 1-4, 5-7, 8-10, and 11-13, respectively. ANU results are for LT 71 km, ICE-6G are for an LT of 120 km (respective best fitting LT).

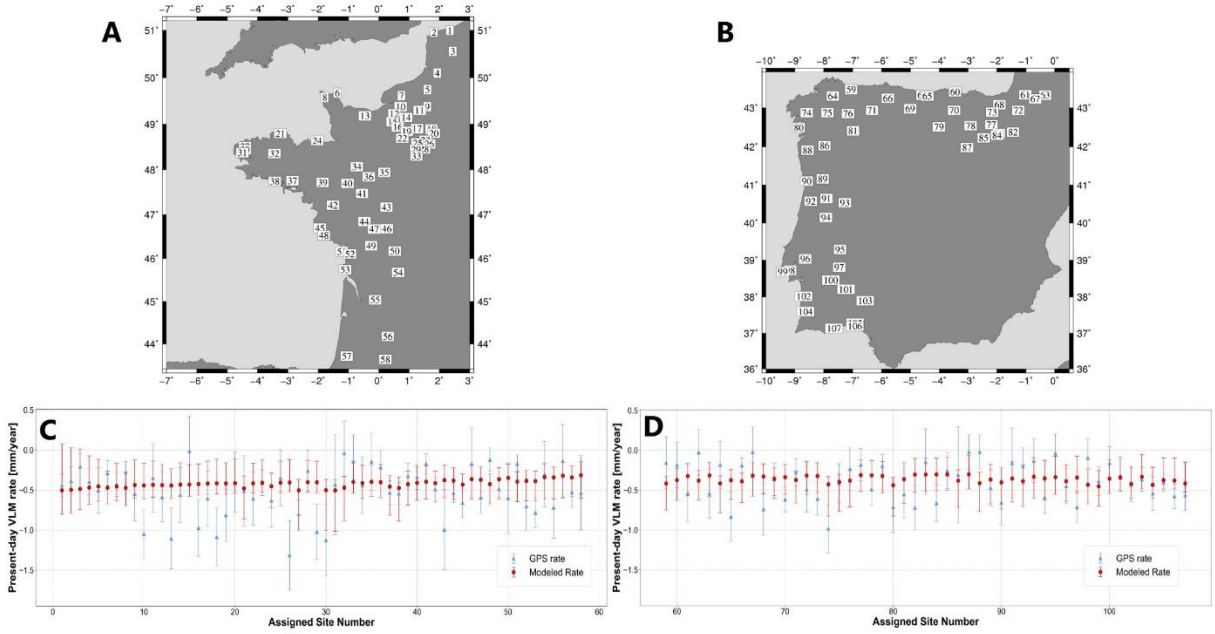

Figure S8. Comparison of rates of VLM predicted by projections for the bestfitting set of Earth parameters (120-p3-50) for ice history model ANU and measured GPS rates.

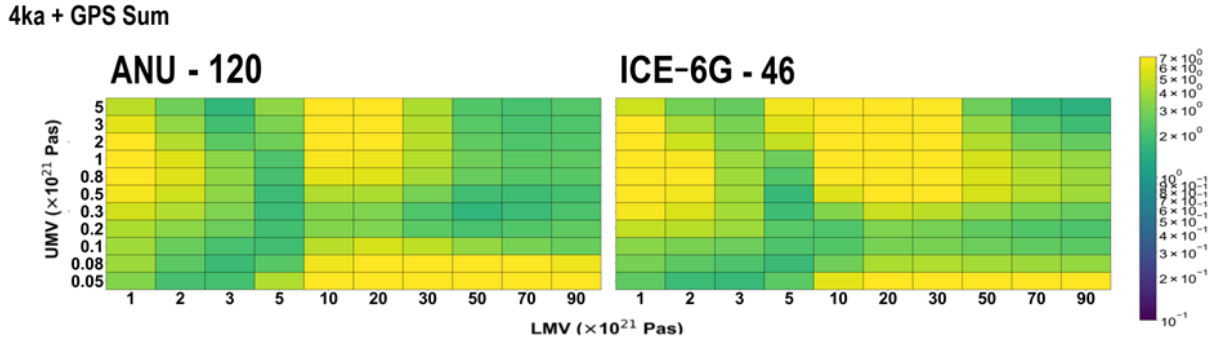

Figure S9. 1σ misfit plot for combined GPS data from stations within 150 km of study area's coast and partial (last 4 cal kyr BP) data as listed. Left: ANU model for LT of 120 km, Right: ICE-6G model for LT of 46 km.

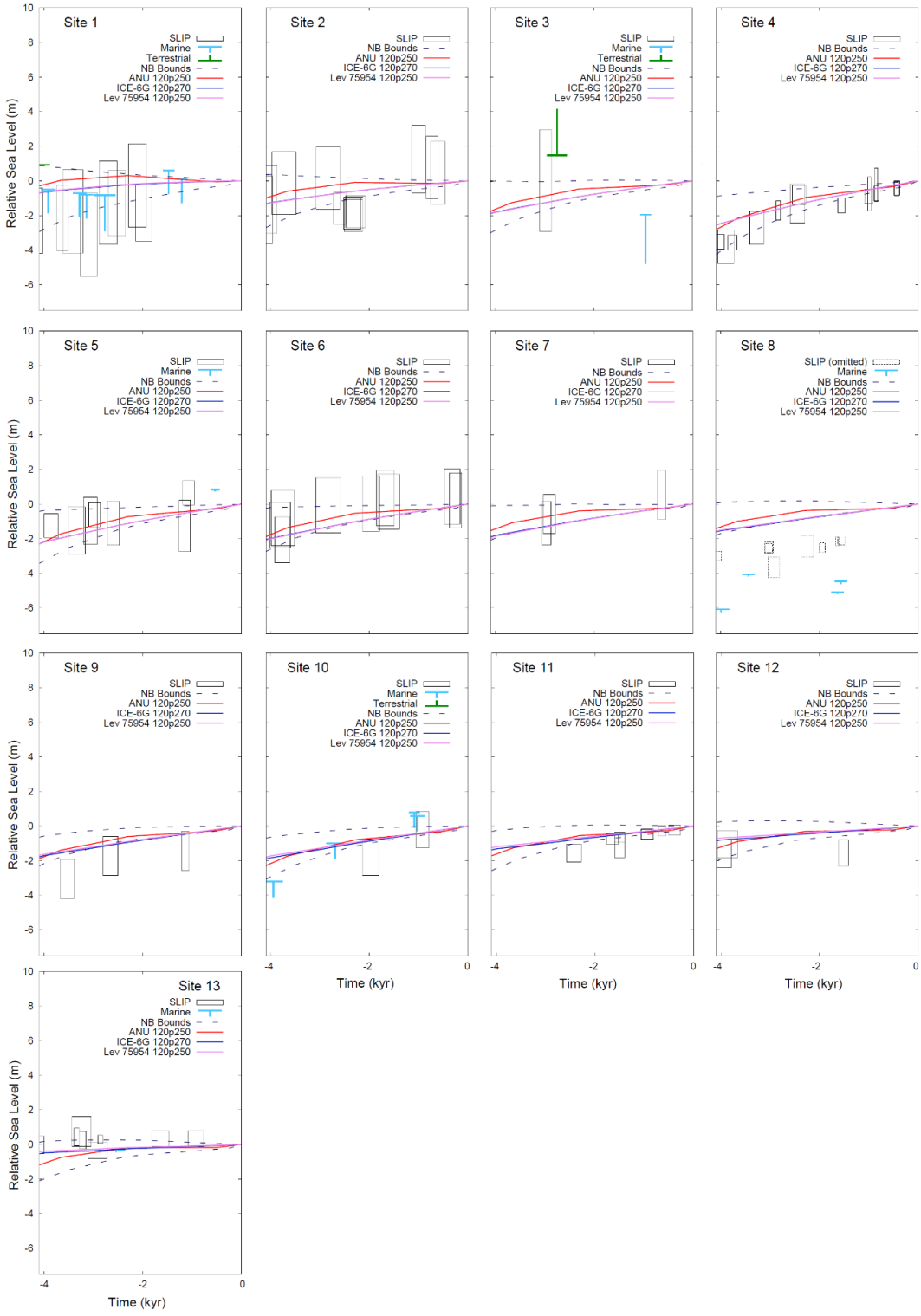

Figure S10. Data-model comparison by sites for RSL dataset and optimal Earth model parameters for the portion of the data set since 4 cal. kyr BP for three ice models: ANU, ICE-6G, and 75954 (see key for details).

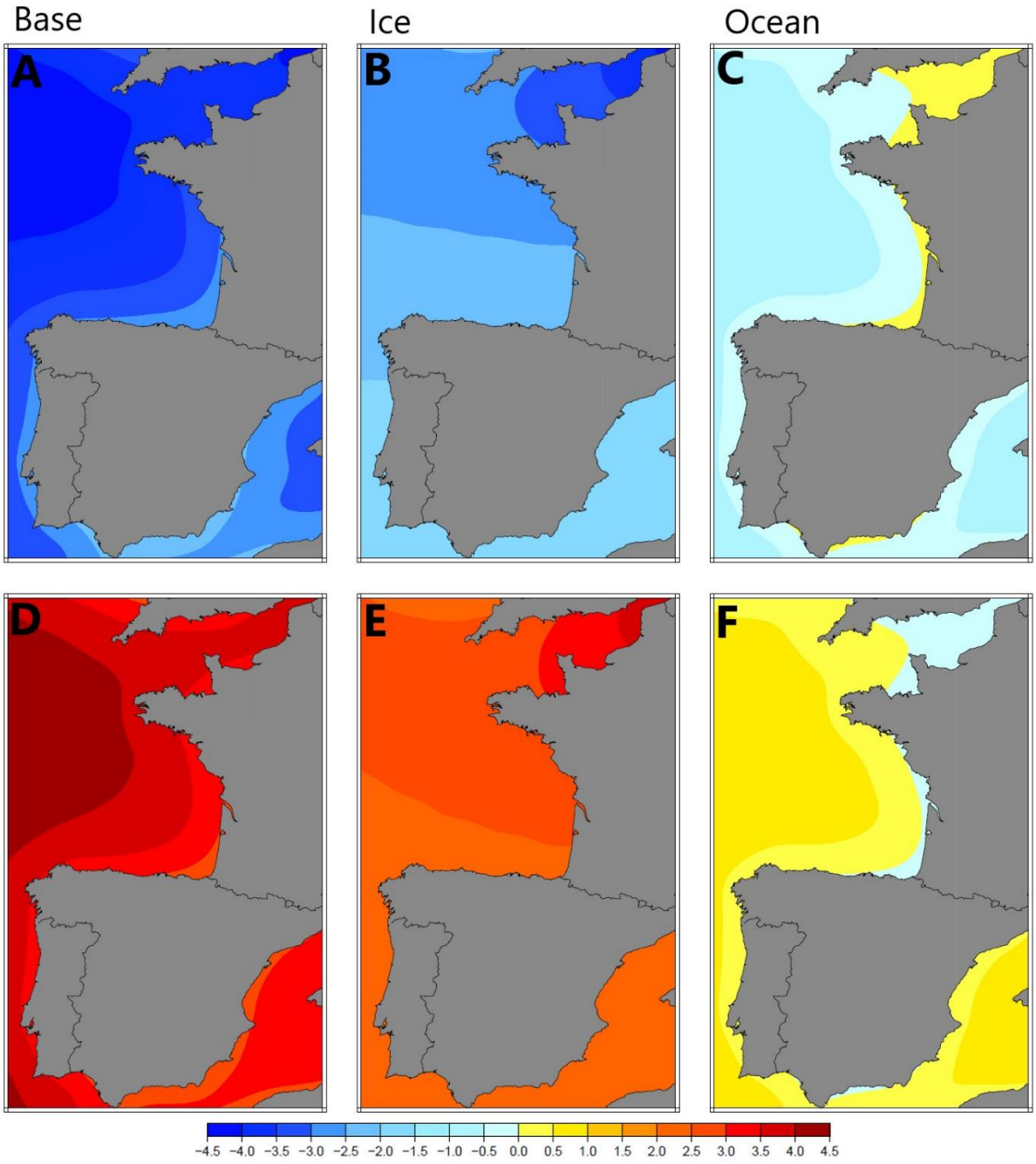

Figure S11. Model output of RSL (top row; A-C) and relative land height (bottom row; D-E) at 6.8 ka for the FIS ice model and Earth model parameter set 71-5-70. Results are provided for the total signal (A, D) as well as that associated with only ice (B, E) or ocean (C, F) loading. Units are in metres.

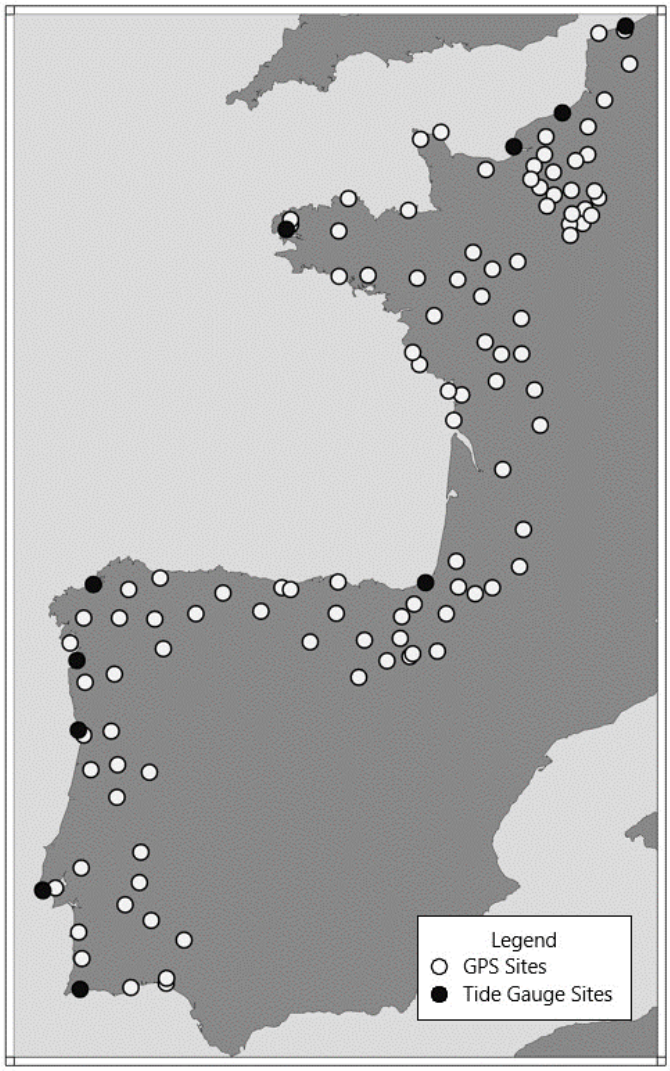

Figure S12. Locations of GPS sites included in this study and of tide gauge stations deemed admissible.

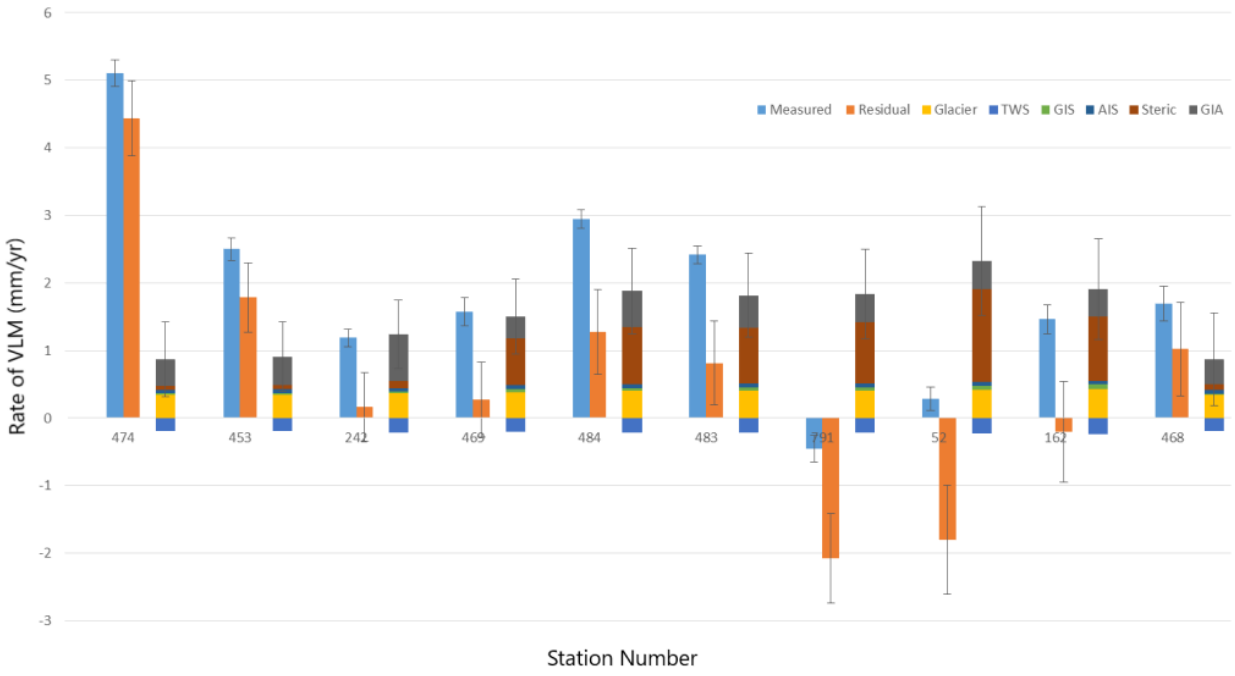

Figure S13. Comparison of components of RSL signal to "Measured" (observed signal at tide gauge station) and residual (observed value with components subtracted).

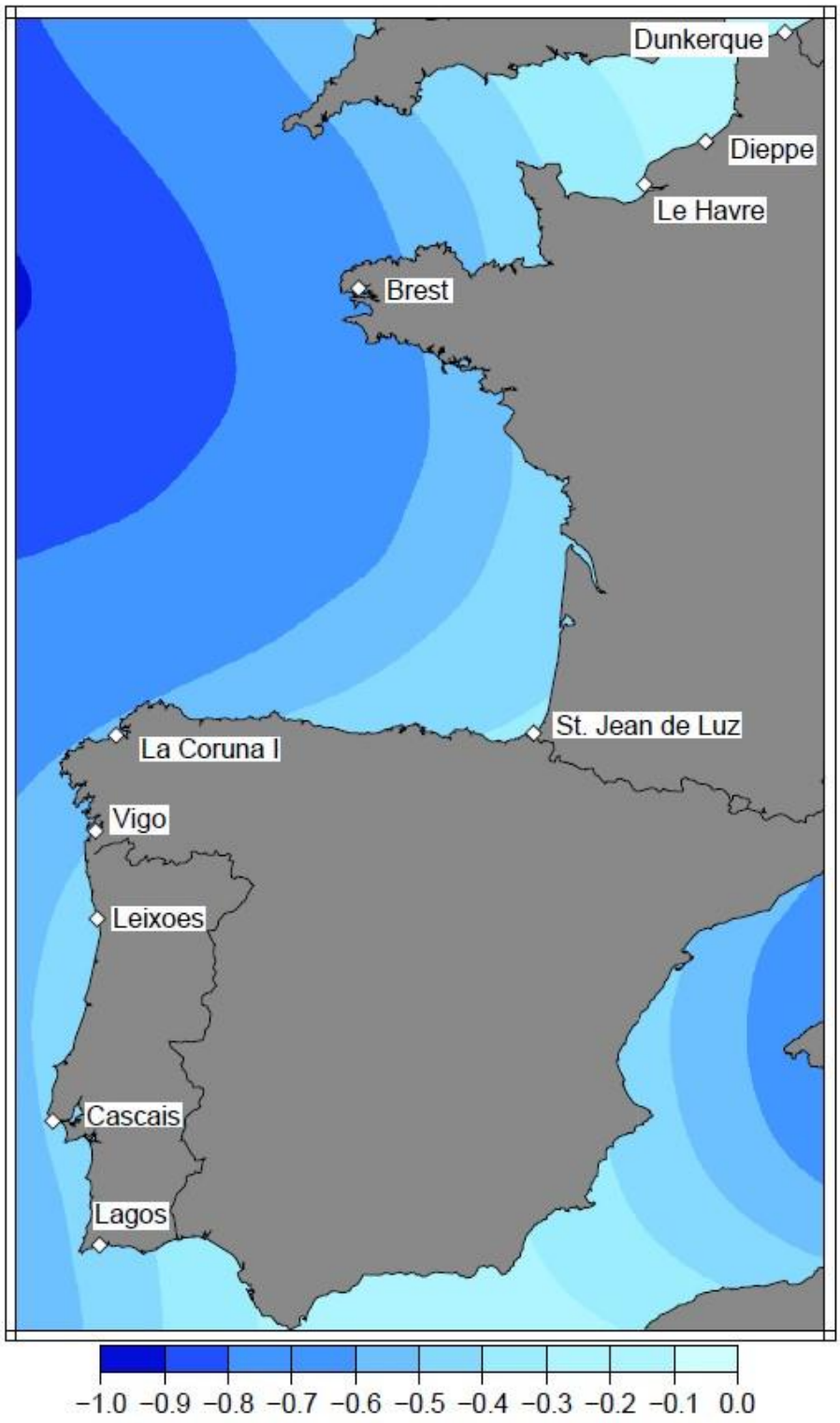

Figure S14. Modelled rates of present-day VLM based on ice history model ANU with the Earth model parameters 120-p3-50, tide gauges used in this study are labelled white diamonds. Units are in mm/year.